AGU PUBLICATIONS

JGR

Journal of Geophysical Research: Solid Earth

RESEARCH ARTICLE

10.1002/2014JB011642

Key Points:
- Relations between source dimensions and corner frequencies are established
- Stress drop estimates are affected by differences in source characteristics
- A small number of receivers produce biased estimates of stress drops and energy

Correspondence to:
Y. Kaneko,
y.kaneko@gns.cri.nz

Citation:
Kaneko, Y., and P. M. Shearer (2015), Variability of seismic source spectra, estimated stress drop, and radiated energy, derived from cohesive-zone models of symmetrical and asymmetrical circular and elliptical ruptures, *J. Geophys. Res. Solid Earth*, *120*, doi:10.1002/2014JB011642.

Received 25 SEP 2014
Accepted 7 DEC 2014
Accepted article online 11 DEC 2014

Variability of seismic source spectra, estimated stress drop, and radiated energy, derived from cohesive-zone models of symmetrical and asymmetrical circular and elliptical ruptures

Y. Kaneko[1] and P. M. Shearer[2]

[1]GNS Science, Lower Hutt, New Zealand, [2]Institute of Geophysics and Planetary Physics, Scripps Institution of Oceanography, University of California, San Diego, La Jolla, California, USA

Abstract Large variability of earthquake stress drops and scaled energy has been commonly reported in the literature, but it is difficult to assess how much of this variability is caused by underlying physical source processes rather than simply observational uncertainties. Here we examine a variety of dynamically realistic rupture scenarios for circular and elliptical faults and investigate to what extent the variability in seismically estimated stress drops and scaled energy comes from differences in source geometry, rupture directivity, and rupture speeds. We numerically simulate earthquake source scenarios using a cohesive-zone model with the small-scale yielding limit, where the solution approaches a singular crack model with spontaneous healing of slip. Compared to symmetrical circular source models, asymmetrical models result in larger variability of estimated corner frequencies and scaled energy over the focal sphere. The general behavior of the spherical averages of corner frequencies and scaled energy in the subshear regime extends to the supershear regime, although shear Mach waves generated by the propagation of supershear rupture lead to much higher corner frequency and scaled energy estimates locally. Our results suggest that at least a factor of 2 difference in the spherical average of corner frequencies is expected in observational studies simply from variability in source characteristics almost independent of the actual stress drops, translating into a factor of 8 difference in estimated stress drops. Furthermore, radiation efficiency estimates derived from observed seismic spectra should not be directly interpreted as describing rupture properties unless there are independent constraints on rupture speed and geometry.

1. Introduction

Understanding the mechanisms responsible for the observed complexities of earthquake source processes is an important, yet difficult task. One way to quantify earthquake source complexity is to estimate stress drop and/or scaled energy (i.e., the ratio of radiated energy to the seismic moment) and analyze their scaling relations. Observational studies suggest that the mean of stress drops for crustal earthquakes is in the range of 1 to 10 MPa and is independent of their magnitude [e.g., *Kanamori and Anderson*, 1975]. Yet stress drops for similar size earthquakes exhibit large scatter, even in relatively compact regions [e.g., *Abercrombie*, 1995; *Shearer et al.*, 2006; *Allmann and Shearer*, 2007]. Similarly, estimates of scaled energy have large scatter, and as a result, the relationship between scaled energy and seismic moment remains a subject of active debate [e.g., *Abercrombie*, 1995; *Mayeda and Walter*, 1996; *Ide et al.*, 2003; *Prieto et al.*, 2004; *Walter et al.*, 2006; *Baltay et al.*, 2011].

It is generally difficult to assess how much of the variability in inferred stress drops and scaled energy is caused by underlying physical source processes or may simply reflect observational uncertainties, such as inaccurate corrections for attenuation and measurement bias due to a limited number of seismic observations. Large variability in stress drops and scaled energy leads to large uncertainties in ground motion prediction, hampering accurate hazard estimation [e.g., *Cotton et al.*, 2013]. In this work, we investigate the origin of variability in inferred stress drops and scaled energy using relatively simple but realistic models of earthquake rupture.

Stress drop is proportional to the ratio of total slip to rupture size. From the classical work of *Eshelby* [1957], stress drop $\Delta\sigma$ for an elliptical crack in a homogeneous elastic medium can be expressed as

$$\Delta\sigma = C(a, b, \nu)\frac{M_0}{bS}\ , \tag{1}$$

©2014. American Geophysical Union. All Rights Reserved.

where $C(a, b, \nu)$ is a geometrical parameter that depends on the major and minor axes a and b of the ellipse [*Madariaga*, 1977] and Poisson's ratio ν, M_0 is the seismic moment, and S is the source area (Appendix A). In the special case of a circular source within a Poissonian solid (i.e., $\nu = 0.25$), the above expression simplifies to

$$\Delta\sigma = \frac{7}{16}\frac{M_0}{a^3} \quad \text{with } a = b \ . \tag{2}$$

Since the physical size of the source is typically inaccessible to direct observation, $\Delta\sigma$ is commonly estimated from far-field body wave spectra using measurements of corner frequencies f_c and a theoretical model of rupture behavior. By assuming a theoretical rupture model, the source radius can be related to the spherical average of corner frequencies $\bar{f}_c$ of body wave seismic spectra through [e.g., *Brune*, 1970; *Madariaga*, 1976; *Kaneko and Shearer*, 2014]

$$\bar{f}_c = k\frac{\beta}{a} \ , \tag{3}$$

where β is the shear wave speed near the source and k is a constant that relates to the spherical average of corner frequencies for a specific theoretical model. From equations (2) and (3), the stress drop $\Delta\sigma$ can be estimated from far-field body wave spectra using spherically averaged measurements of corner frequency $\bar{f}_c$, together with seismic moment M_0 determined from the low-frequency part of the spectra:

$$\Delta\sigma = \frac{7}{16}\left(\frac{\bar{f}_c}{k\beta}\right)^3 M_0 \ . \tag{4}$$

Clearly, any uncertainty in $\bar{f}_c$, k, or β is cubed when computing stress drop.

The value of k in equation (3) depends on which theoretical relationship is used to relate corner frequency and source radius. Many investigators [e.g., *Hanks and Thatcher*, 1972; *Archuleta et al.*, 1982; *Ide et al.*, 2003; *Baltay et al.*, 2011; *Cotton et al.*, 2013; *Oth and Kaiser*, 2014] used the model of *Brune* [1970], who assumed a simple but somewhat ad hoc kinematic model for a circular fault and obtained $k = 0.37$ for S waves. Others [e.g., *Prejean and Ellsworth*, 2002; *Stork and Ito*, 2004; *Imanishi and Ellsworth*, 2006] applied the analytical model of *Sato and Hirasawa* [1973] in which the rupture initiates at a point, spreads radially with a constant rupture speed, and then stops abruptly at the source radius. This model assumes that the static solution of *Eshelby* [1957] holds at every successive instant of rupture formation under uniform stress, in which case k depends on the rupture speed V_r with $k^p = 0.42$ for P waves and $k^s = 0.29$ for S waves for $V_r = 0.9\beta$. An unphysical feature of the model of *Sato and Hirasawa* [1973] is that particle motion ceases instantly at the same time, everywhere over the fault plane.

The model of *Madariaga* [1976] has been widely used [e.g., *Abercrombie*, 1995; *Prieto et al.*, 2004; *Abercrombie*, 2005; *Shearer et al.*, 2006; *Allmann and Shearer*, 2007, 2009; *Yang et al.*, 2009; *Yamada et al.*, 2010]. *Madariaga* [1976] performed finite-difference calculations for a singular crack radially expanding at a constant speed and found that $\bar{f}_c = k\beta/a$, where $\bar{f}_c$ is the spherically averaged corner frequency, β is the shear wave speed, a is the radius of the circular source, and $k = 0.32$ and 0.21 for P and S waves, respectively, assuming the rupture speed $V_r = 0.9\beta$. Since stress in the Madariaga model is singular at the rupture front, the finite mesh size and smoothing procedures affect the resulting corner frequencies. To remedy this problem, *Kaneko and Shearer* [2014] considered cohesive-zone models of a circular fault with the small-scale yielding limit and numerically found that the values of k for the singular crack model with spontaneous healing of slip are actually larger than the prediction of *Madariaga* [1976], with $k = 0.38$ for P waves and $k = 0.26$ for S waves for the rupture speed $V_r = 0.9\beta$.

A key issue we address here is the validity of the standard assumption of a symmetrical circular source applied to real earthquakes. Observational studies hint that most ruptures of large crustal events are predominantly unilateral [e.g., *Henry and Das*, 2001; *McGuire et al.*, 2002]. Since source geometry, directivity, and rupture speeds for small earthquakes are generally harder to constrain, stress drop estimation often relies on one of the above mentioned theoretical models with the rupture expanding radially at a constant speed until it encounters the periphery of the circular source. Such models are clearly an oversimplification of earthquake rupture processes in nature. Hence, we expect that some degree of variability in inferred stress

©2014. American Geophysical Union. All Rights Reserved.

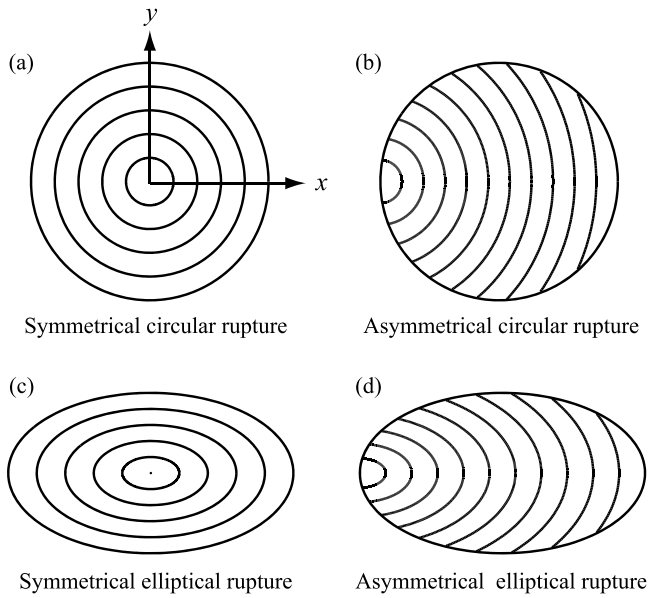

Figure 1. Source scenarios considered in this study. (a) Symmetrical circular source where the rupture nucleates at the center, grows circularly with a constant rupture speed, and stops at the edge. Contours correspond to rupture arrival times on the fault. (b) Asymmetrical circular source where the rupture nucleates at one end and propagates mostly unilaterally at a constant rupture speed and stops at the edge of the circular fault. (c) Symmetrical elliptical source where the rupture grows at different speeds along the *x* and *y* directions. (d) Asymmetrical elliptical source where the rupture nucleates at one end and propagates mostly unilaterally at a constant rupture speed and stops at the edge of the elliptical fault.

drops comes from variability in source geometry, rupture directivity, and rupture speeds that are independent of the actual stress drop.

In the classical circular rupture models, the center of the expanding circular front coincides with the center of the fault, which is referred to as an "symmetrical" model as opposed to an "asymmetrical" model where the above two points are different [*Dong and Papageorgiou*, 2003]. *Boatwright* [1981] numerically analyzed far-field radiation of asymmetrical models and found stronger directivity effects compared to that of the symmetrical model. *Dong and Papageorgiou* [2002a, 2003] extended the results of *Burridge and Willis* [1969] and derived closed-form analytical solutions of the far-field radiation for asymmetrical and elliptical ruptures propagating at subshear speeds, generalizing the circular fault model of *Sato and Hirasawa* [1973].

In this work, we attempt to quantify to what extent the variability in estimated stress drops and scaled energy may arise from differences in source geometry, rupture directivity, and rupture speeds. We study far-field body wave spectra derived from source models with different fault geometries and rupture behavior. We consider four general source scenarios (Figure 1): (i) symmetrical circular rupture where the center of the expanding front coincides with the center of the circular fault, (ii) asymmetrical circular rupture where the hypocenter is located on the periphery of a circular fault, (iii) symmetrical elliptical rupture where the rupture propagates at different speeds in different directions, and (iv) asymmetrical elliptical rupture. A primary motivation for considering elliptical rupture is to extend the analysis of *Kaneko and Shearer* [2014] to supershear rupture, where the rupture speed can exceed the local *S* wave speed along the Mode II direction, but not along the Mode III direction [e.g., *Burridge*, 1973; *Andrews*, 1976].

To obtain the corner frequencies of radiated body waves for earthquakes with various fault geometry, we use dynamic models of expanding rupture where the rupture propagates over the prescribed source area at a constant speed and the slip spontaneously arrests due to the arrivals of stopping phases. We consider simple classes of circular and elliptical rupture models that are physically realizable, i.e., have no stress singularities, and that are generated by simulations with a proper numerical resolution. For each rupture scenario, we analyze the behavior of seismic body wave spectra, the relation between the corner frequency and the source radius, the variations of estimated corner frequencies and scaled energy over the focal sphere, and the dependence of these parameters on the rupture speeds. We discuss uncertainties in estimation of stress drop and scaled energy and the implications of our results for the large variability reported in previous observational work (section 8).

2. Cohesive-Zone Model of an Elliptical Fault

We consider circular and elliptical faults embedded in an infinite homogeneous, isotropic elastic medium (Figure 2a). The degree of ellipticity of the elliptical source is quantified by its "eccentricity" ε with major and

©2014. American Geophysical Union. All Rights Reserved.

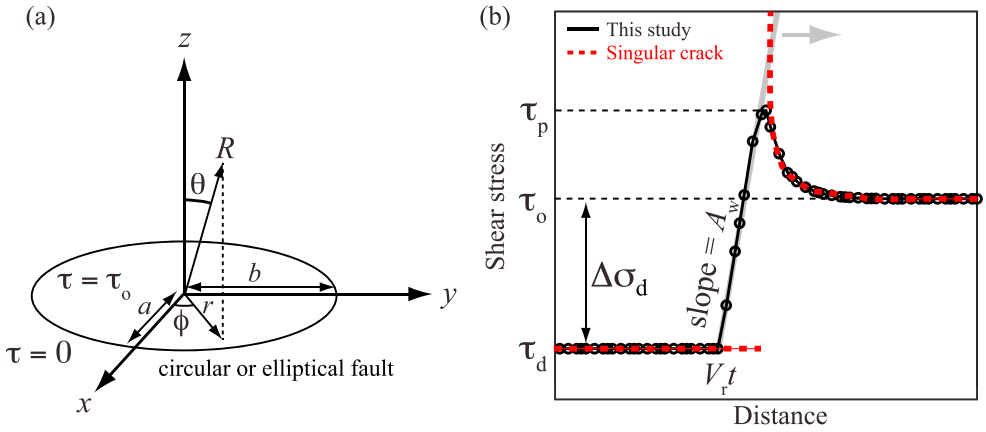

Figure 2. Model geometry and fault constitutive response. (a) A circular fault with radius a or an elliptical fault with major axis a and minor axis b embedded in an infinite medium. Prestress τ_o is uniform over the fault patch and zero outside. (b) Fracture criterion used in this study and that for the singular crack assumed in *Madariaga* [1976]. In our study, fault strength increases linearly from $|\mathbf{r}| = V_r t$ (as shown by a gray line) within the cohesive zone. Slip begins when the shear stress τ on the fault reaches the shear strength τ_p.

minor axes a and b:

$$\varepsilon = \sqrt{1 - \left(\frac{b}{a}\right)^2}. \tag{5}$$

For $\varepsilon = 0$, we obtain a circular fault, whereas an elongated fault can be obtained by making $0 < \varepsilon < 1$.

To create a source model closely related to singular crack models of expanding rupture [e.g., *Sato and Hirasawa*, 1973; *Madariaga*, 1976; *Dong and Papageorgiou*, 2003], we follow the procedure used in the earlier studies [*Andrews*, 1985; *Dunham and Bhat*, 2008] in which the shear strength τ_{st} of the fault weakens linearly at a rate A_w with distance within the cohesive zone:

$$\tau_{st} = \max\{\tau_d, \tau_d + A_w(|\mathbf{r}| - V_r t)\}, \tag{6}$$

where τ_d is dynamic shear strength, $|\mathbf{r}| = \sqrt{x^2 + y^2}$, and V_r is the rupture speed (Figure 2b). For an expanding elliptical rupture, the rupture speed V_r in equation (6) may be expressed as

$$V_r = V_x V_y \left(\frac{x^2 + y^2}{V_y^2 x^2 + V_x^2 y^2}\right)^{1/2}, \tag{7}$$

where V_x and V_y are the rupture speeds along the major and minor axes, respectively. The fault stressed initially at τ_o does not move until the shear stress reaches the fault strength τ_p, which is not specified a priori, but depends on the dynamic strength τ_d and the weakening rate A_w (Figure 2b). The shear stress is always equal to the shear strength during the sliding but can be smaller than the shear strength (i.e., stress overshoot) after the sliding terminates.

In this model, the rupture nucleates at a point within the source area S, and the rupture front expands radially by maintaining its elliptical shape (i.e., constant ε). Fault growth stops instantaneously as the rupture runs into the zone of zero shear stress outside the source region. The level of shear stress outside of the source region can be arbitrary as long as it is much smaller than the dynamic strength τ_d. In the limit where the weakening rate A_w becomes infinitely large (i.e., the small-scale yielding limit), the model approaches a singular crack model (Figure 2b). Note that equation (6) is different from the commonly used slip-weakening friction law, where the resulting rupture becomes spontaneous, leading to a more complex source model with set of complicated waveforms. For simplicity, we fix the rupture speeds V_x and V_y as constant in time, but the model is still dynamic in the sense that we solve for the fault motion given the rupture speeds and prescribed dynamic stress drop $\Delta\sigma_d$ (sometimes called effective stress).

We solve the elastodynamic equation coupled with the fracture criterion (equation (6)) using a spectral element method [*Komatitsch and Vilotte*, 1998; *Kaneko et al.*, 2008, 2011]. We choose a large enough computational domain such that waves reflected by the domain boundaries do not propagate back to the

©2014. American Geophysical Union. All Rights Reserved.

source area. For simplicity, only the x components of slip and shear traction are solved numerically; there is no rake rotation as the elliptical rupture front advances. To produce well-resolved numerical results, we ensure that there are at least 7 to 10 computational node points within a cohesive zone. The spectral element model incorporates artificial viscosity of the Kelvin-Voight form to suppress spurious oscillations generated by the fault slip at frequencies that are too high to be resolved by the mesh (Appendix B). The dynamic rupture code has been verified through the Southern California Earthquake Center Dynamic Rupture Code Verification Exercise [*Harris et al.*, 2009, 2011].

A dimensional analysis of the problem allows for the representation of solutions in terms of nondimensional variables. We choose the following nondimensionalizations similar to those in *Kaneko and Shearer* [2014]:

$$\text{Length} \quad r' = r/\sqrt{ab} \tag{8}$$

$$\text{Time} \quad t' = t\beta/\sqrt{ab} \tag{9}$$

$$\text{Stress} \quad \sigma'_{ij} = \sigma_{ij}/\Delta\sigma_{\mathrm{d}} \tag{10}$$

$$\text{Displacement} \quad u'_{\mathrm{i}} = u_{\mathrm{i}}\mu/(\Delta\sigma_{\mathrm{d}}\sqrt{ab}) \tag{11}$$

$$\text{Weakening rate} \quad A'_{\mathrm{w}} = A_{\mathrm{w}}\sqrt{ab}/\Delta\sigma_{\mathrm{d}} \tag{12}$$

$$\text{Seismic moment} \quad M'_0 = M_0/(\Delta\sigma_{\mathrm{d}}(ab)^{3/2}) \tag{13}$$

$$\text{Fracture energy per unit area} \quad G' = G\mu/(\Delta\sigma_{\mathrm{d}}^2\sqrt{ab}) \tag{14}$$

$$\text{Radiated energy} \quad E'_{\mathrm{r}} = E\mu/(\Delta\sigma_{\mathrm{d}}^2(ab)^{3/2}) , \tag{15}$$

where nondimensional variables are denoted by a prime. The physical variables include the major and minor axes a and b of an elliptical source, the dynamic stress drop $\Delta\sigma_{\mathrm{d}}$, the S wave speed β, and the shear modulus μ. We assume that the Poisson's ratio is 0.25 such that $\alpha = \sqrt{3}\beta$.

3. Symmetrical Circular Rupture

In this section, we describe the procedure for computing the spherical average of normalized corner frequencies k in equation (3) for each source scenario. We then summarize the characteristics of the symmetrical circular source already discussed in *Kaneko and Shearer* [2014] to facilitate comparisons with more complex source scenarios considered in this work. For each model with a given rupture speed, we report k values, stress drop, scaled energy, radiation efficiency, and the S-to-P radiated energy ratio, most of which were not reported in *Kaneko and Shearer* [2014].

We simulate an earthquake source using a cohesive-zone model with the small-scale yielding limit, where the cohesive-zone size becomes much smaller than the source dimension and the solution approaches a singular crack model with spontaneous healing of slip (Figure 3). In this limit, the resulting corner frequencies are independent of the rate of frictional weakening A'_{w} and the dynamic stress drop $\Delta\sigma_{\mathrm{d}}$, and hence, for a prescribed rupture speed, we can obtain unique values of P and S wave normalized corner frequencies k_p and k_s, respectively [*Kaneko and Shearer*, 2014].

Using the source time histories of the rupture model, we compute far-field body wave displacement over the focal sphere for a homogeneous elastic whole space. Far-field body wave displacement radiated by a shear dislocation at an individual fault patch can be expressed as

$$\mathbf{u}(\mathbf{x},t) = \frac{1}{4\pi\rho\alpha^3}\mathbf{A}^p\frac{1}{R}\dot{M}_{\mathrm{o}}\left(t-\frac{R}{\alpha}\right) + \frac{1}{4\pi\rho\beta^3}\mathbf{A}^s\frac{1}{R}\dot{M}_{\mathrm{o}}\left(t-\frac{R}{\beta}\right) , \tag{16}$$

where ρ is the density, $\dot{M}_{\mathrm{o}}$ is the moment rate, R is the distance from the dislocation source to a receiver, and $\mathbf{A}^p$ and $\mathbf{A}^s$ are radiation pattern terms for far-field P and S waves, respectively [*Aki and Richards*, 2002, equation (4.32)]. Note that the notation is slightly different from that in *Kaneko and Shearer* [2014]. We then sum $\mathbf{u}(\mathbf{x},t)$ at a receiver for contributions from all the source grid points to account for the finiteness of the simulated source. As a test of both the numerical solution and the representation theorem approach, we have verified that both produce the same seismograms at close distances to the source (in this case we retained the near-field terms in *Aki and Richards* [2002]). To focus only on source properties, we assume no attenuation or scattering in computing our synthetic seismograms.

©2014. American Geophysical Union. All Rights Reserved.

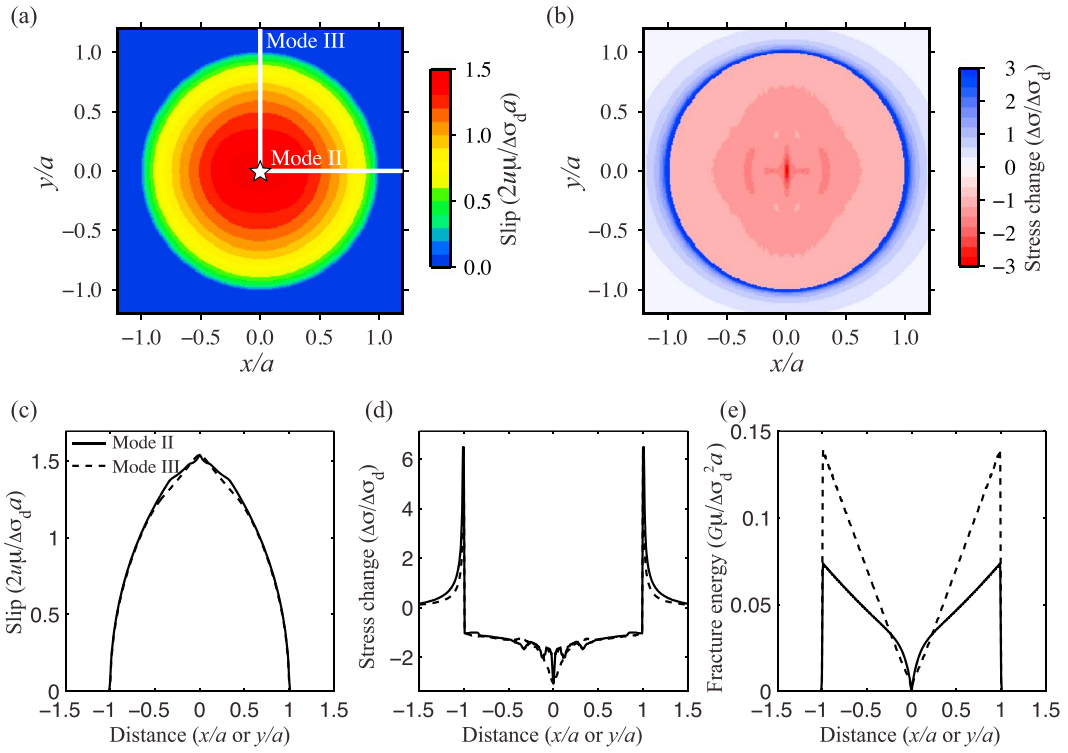

Figure 3. Characteristics of a symmetrical circular source with the rate of frictional weakening $A'_w = 84$ and the rupture speed $V_r/\beta = 0.9$. (a) Final slip distribution and (b) the corresponding stress-change distribution on the fault. White star indicates the hypocenter. (c–f) The profiles of slip S', stress change $\Delta\sigma'$, and fracture energy G' along x (solid) and y (dashed) directions.

The corresponding spectrum is obtained by taking the Fourier transform of the magnitude of the far-field displacement $|\mathbf{u}(\mathbf{x}, t)|$ at each receiver. The corner frequency and spectral fall-off rate are estimated using common procedures in observational work. We fit a Brune-type spectral function [*Brune*, 1970] given by

$$u(f) = \frac{\Omega_0}{1 + (f/f_c)^n} \tag{17}$$

to an individual spectrum, where Ω_0 is the long-period spectral level, which is proportional to the seismic moment, f_c is the corner frequency, and n is the spectral fall-off rate. The spectral parameters f_c and n are estimated by a least squares fit of the log spectrum with function (17) for $0.05 f_c \lesssim f \lesssim 10 f_c$ using a grid-search method (e.g., Figure 4c). We weight the fit inversely with frequency so that all parts of the spectrum seen in a log-log plot contribute equally. This weighting procedure generally improves the fit to the low-frequency part of the spectrum, which is defined by relatively few points.

The corner frequencies of displacement spectra are computed at takeoff angles sampled every 5° over the focal sphere. The variations of normalized (see below) corner frequencies and spectral fall-off rates are projected on a unit sphere for visualization (Figure 4). Near the equator (or low latitudes), the resulting corner frequencies are generally smaller due to the directivity effect; the difference between wave arrivals from the near side and far side of the fault is larger, resulting in a longer pulse duration and smaller corner frequency (Figures 4a). Spectral fall-off rates are generally larger at higher latitudes (Figures 4b). Although a slight asymmetry comes from different dynamic source behavior along the Mode II and III directions, the corner frequencies for the symmetrical circular model do not display strong azimuthal dependence (Figure 4a). The relations between the spherical average of *P* and *S* corner frequencies and the source radius are found as

$$\bar{f}_c^p = k^p \frac{\beta}{a} = 0.38 \frac{\beta}{a}$$
$$\bar{f}_c^s = k^s \frac{\beta}{a} = 0.26 \frac{\beta}{a} \tag{18}$$

©2014. American Geophysical Union. All Rights Reserved.

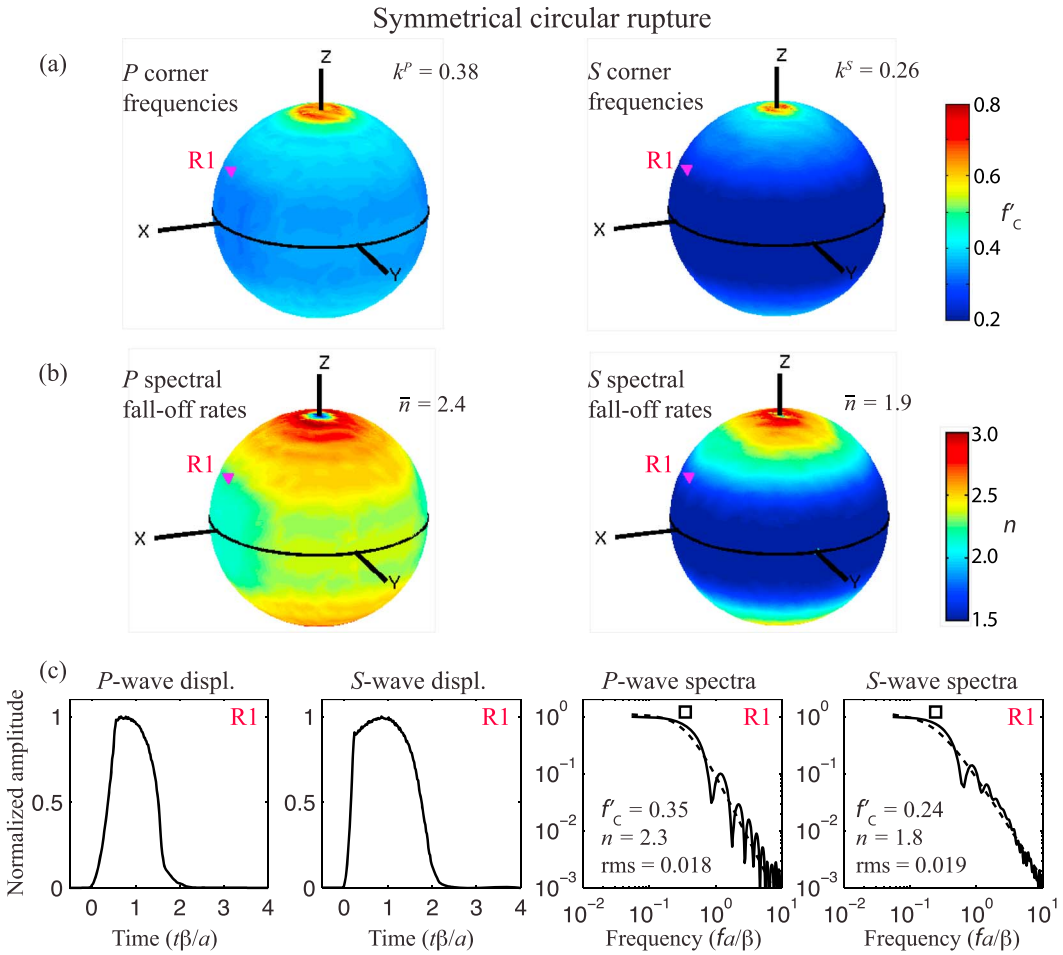

Figure 4. Far-field displacements, spectra, and corner frequencies f'_c for a symmetrical circular model with rupture speed $V_r/\beta = 0.9$. (a) Variations of *P* and *S* wave f'_c over the focal sphere. The black circle on the *x*-*y* plane is parallel to the fault surface. The values of k^P and k^S (i.e., the spherical average of f'_c) are indicated. (b) Variations of *P* and *S* spectral fall-off rates over the focal sphere. The spherical average of fall-off rates $\bar{n}$ is indicated. (c) Magnitude of far-field displacement and spectra at receiver R1. Dashed lines show the best fitting model of equation (17) with fall-off rate *n*, root-mean-square error (RMS), and corner frequency f'_c (open square).

for the symmetrical circular source with the rupture speed $V_r = 0.9\beta$. The *k* values are the corner frequencies normalized by the shear velocity β and source dimension *a*, and we will sometimes refer to *k* as normalized corner frequency when comparing the results of different source scenarios. As discussed in *Kaneko and Shearer* [2014], the values of *k* in (18) are larger than those in the Madariaga model by 19% for *P* waves and 24% for *S* waves, respectively. They are smaller than those of *Sato and Hirasawa* [1973] with $k^P = 0.42$ and $k^S = 0.29$ because the source duration of the cohesive-zone model is longer, due to the spontaneous healing of slip, than that of *Sato and Hirasawa* [1973]. The values of *k* for both *P* and *S* waves are larger for models with faster rupture speeds (Table 1), consistent with the results of *Sato and Hirasawa* [1973]. The *P*-to-*S* corner frequency ratio k^P/k^S is also larger for models with a faster rupture speed.

The resulting stress drop $\Delta\sigma$, scaled energy E'_r/M'_0, and radiation efficiency $\eta_{\text{eff}} = 2\mu E_r/(\Delta\sigma M_0)$ for each source scenario are shown in Table 1. The stress drop based on equation (2) increases slightly with the rupture speed V_r but generally remains almost independent of V_r (Table 1). The radiated energy E_r of the source model can be computed via [e.g., *Kostrov*, 1974; *Ma and Archuleta*, 2006]

$$E_r = \int_\Sigma \frac{\tau^o(\xi) + \tau^f(\xi)}{2} D(\xi) d\Sigma - \int_0^\infty \int_\Sigma \tau(\xi, t) V(\xi, t) \mathrm{d}\Sigma \mathrm{d}t \,, \tag{19}$$

where τ^o is the initial shear stress, τ^f is the final shear stress, *D* is the slip, *V* is the slip rate, and Σ is the source area. We find that E'_r/M'_0 is larger for models with a faster rupture speed (Table 1), also consistent with the

©2014. American Geophysical Union. All Rights Reserved.

Table 1. Source Parameters for All the Rupture Models Considered in This Study[a]

	$\frac{V_r}{\beta}$	k^p	k^s	$\frac{k^p}{k^s}$	$\frac{\Delta\sigma}{\Delta\sigma_d}$	$\frac{E'_r}{M'_0}$	η_{eff}	$\frac{E^s_r}{E^p_r}$	k^p_{stack}	k^s_{stack}	$k^p_{n=2}$	$k^s_{n=2}$	k^p_{Snoke}	k^s_{Snoke}
Sym. circ.	0.6	0.30	0.25	1.2	1.21	0.12	0.20	17	0.31	0.28	0.23	0.21	0.31	0.26
	0.7	0.32	0.26	1.2	1.23	0.16	0.26	17	0.34	0.30	0.25	0.24	0.33	0.29
	0.8	0.35	0.26	1.3	1.24	0.20	0.34	18	0.37	0.30	0.27	0.29	0.36	0.32
	0.9	0.38	0.26	1.5	1.26	0.30	0.48	22	0.39	0.29	0.29	0.34	0.38	0.36
Asym. circ.	0.6	0.21	0.20	1.1	1.14	0.059	0.098	24	0.22	0.21	0.19	0.17	0.21	0.20
	0.7	0.24	0.23	1.0	1.17	0.093	0.16	26	0.25	0.25	0.21	0.20	0.24	0.22
	0.8	0.27	0.26	1.0	1.20	0.16	0.26	30	0.27	0.27	0.23	0.24	0.27	0.25
	0.9	0.29	0.28	1.0	1.22	0.30	0.50	37	0.30	0.27	0.26	0.30	0.29	0.29
Sym. ellip.	0.7	0.30	0.24	1.3	1.20	0.095	0.16	19	0.29	0.26	0.21	0.20	0.29	0.24
	0.9	0.34	0.26	1.3	1.23	0.16	0.27	21	0.35	0.29	0.25	0.26	0.33	0.29
	1.3	0.41	0.28	1.5	1.26	0.26	0.41	21	0.43	0.32	0.30	0.31	0.38	0.34
	1.6	0.42	0.28	1.5	1.27	0.31	0.48	18	0.42	0.32	0.35	0.32	0.42	0.36
Asym. ellip.	0.7	0.19	0.19	1.0	1.12	0.062	0.11	33	0.20	0.21	0.17	0.18	0.19	0.19
	0.9	0.25	0.26	0.96	1.16	0.19	0.32	39	0.25	0.27	0.22	0.26	0.24	0.25
	1.3	0.35	0.31	1.1	1.20	0.27	0.45	24	0.37	0.31	0.29	0.30	0.31	0.31
	1.6	0.42	0.33	1.3	1.23	0.30	0.49	12	0.43	0.33	0.39	0.30	0.38	0.33

[a]The results of symmetrical circular source (sym. cir.), asymmetrical circular source (asym. cir.), symmetrical elliptical source (sym. ellip.), and asymmetrical elliptical source (asym. ellip.) are described in sections 3–6, respectively. P and S wave corner frequencies $k^p = \bar{f}^p_c a/\beta$ and $k^s = \bar{f}^s_c a/\beta$, stress drop $\Delta\sigma/\Delta\sigma_d$ (equation (2)), radiated energy to moment ratios E'_r/M'_0, radiation efficiency η_{eff}, and S-to-P radiated energy ratio E^s_r/E^p_r for models with a different rupture speed V_r/β are shown. Corner frequencies k^p and k^s with subscripts "stack" and "$n = 2$" correspond to corner frequencies obtained by stacked spectra and fitting with $n = 2$ to the stacked spectra, respectively. Corner frequency frequencies k^p_{Snoke} and k^s_{Snoke} are calculated using the definition of *Snoke* [1987] (see text). Note that $\Delta\sigma$, E'_r/M'_0, and η_{eff} are computed from dynamic source models directly, whereas the others are estimated from far-field displacements or spectra.

results of *Sato and Hirasawa* [1973]. Since $\Delta\sigma$ is almost independent of V_r, the radiation efficiency η_{eff} is also larger for models with a faster rupture speed (Table 1).

The ratio of S-to-P radiated energy, E^s_r/E^p_r, is another important parameter for understanding the underlying source processes and is often inferred from observations. We estimate the total radiated energy E_r from the far-field body waves using [e.g., *Haskell*, 1964]

$$E_r = E^p_r + E^s_r = 2\rho \int_\Gamma \int_0^\infty \left[\alpha(\dot{u}^p)^2 + \beta(\dot{u}^s)^2\right] df\, d\Gamma \quad \text{for frequency domain} \tag{20}$$

$$E_r = E^p_r + E^s_r = \rho \int_\Gamma \int_0^\infty \left[\alpha(\dot{u}^p)^2 + \beta(\dot{u}^s)^2\right] dt\, d\Gamma \quad \text{for time domain}, \tag{21}$$

where $\dot{u}^p$ and $\dot{u}^s$ are far-field particle velocities for P and S waves, respectively, and Γ is the area over the focal sphere. *Kaneko and Shearer* [2014] found that the estimated radiated energy using the time domain method agrees well with that of the input source model. For a point source model where the P and S wave pulses have identical shapes and hence the same f^p_c and f^s_c, $E^s_r/E^p_r = 23$ for a Poisson solid. For the symmetrical circular model, the time domain method yields $E^s_r/E^p_r = 22$ for $V_r = 0.9\beta$ (Table 1). These values are close to the point source model and also agree fairly well with $E^s_r/E^p_r = 25$ for the circular source model of *Sato and Hirasawa* [1973]. The E^s_r/E^p_r ratio is larger for models with a faster rupture speed, suggesting that the S wave energy is radiated more efficiently for models with faster rupture speeds.

4. Asymmetrical Circular Rupture

To illustrate the influence of rupture directivity on the corner frequencies of far-field body waves, we consider a source model where the rupture nucleates at the periphery of the circular fault and propagates to the other end. As in the symmetrical circular model, we assume that the rupture expands radially

©2014. American Geophysical Union. All Rights Reserved.

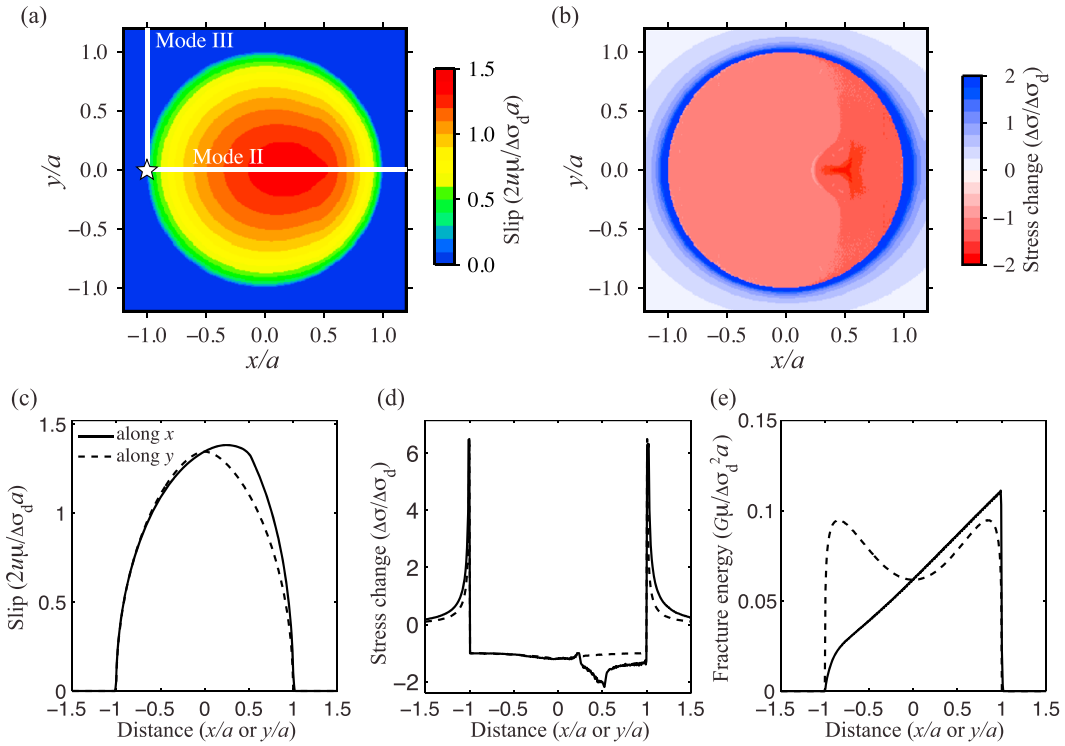

Figure 5. Characteristics of an asymmetrical circular source with the rate of frictional weakening $A'_w = 84$ and the rupture speed $V_r/\beta = 0.9$. (a) Final slip distribution and (b) the corresponding stress-change distribution on the fault. White star indicates the hypocenter. (c–f) The profiles of slip S', stress change $\Delta\sigma'$, and fracture energy G' along x (solid) and y (dashed) directions.

outward until it encounters the edge of the circular source, and hence, the rupture mostly propagates unilaterally (Figure 1b). The stopping phases are continuously generated as the rupture front reaches the periphery of the source region. This assumption is different from the asymmetrical rupture model of *Dong and Papageorgiou* [2002a] where the rupture simultaneously arrests at the circular periphery of the source.

Slip and stress drop distributions for a representative model are shown in Figure 5. Compared to the symmetrical circular model (Figure 3), the asymmetrical model leads to asymmetrical slip and stress distributions. As in the symmetrical model, the fracture energy monotonically increases with distance away from the hypocenter (Figures 5e). The actual stress drop is similar to the dynamic stress drop $\Delta\sigma_d$ in the region near the hypocenter but is larger by up to a factor of 2 in some parts of the source region (Figures 5b and 5d). The stopping phases generated at the periphery of the source region propagate over the fault incoherently, and consequently, the stress overshoot averaged over the source region is slightly smaller than that in the symmetrical circular model.

The corresponding far-field displacement pulses and their spectra are shown in Figure 6. The displacement pulses for the asymmetrical model are quite different from those of the symmetrical model and show larger variability in the shape of the displacements over the focal sphere. Unlike the symmetrical circular model (Figure 4), the asymmetrical model displays a strong azimuthal dependence due to the asymmetry of the rupture evolution, or the directivity effect (Figure 6). It is evident from Figure 6a that the corner frequencies are larger in the region along the direction of rupture propagation (e.g., at receiver R1 in Figure 6) than the region from which the rupture propagates away (e.g., at receiver R2). The directivity effect is stronger for S waves than P waves because the rupture speed $V_r/\beta = 0.9$ is closer to the S wave speed than the P wave speed (Figure 6a). The spectral fall-off rates n show more complex patterns, with n ranging from 1.9 to 2.8 and 1.5 to 3.0 for P and S waves, respectively (Figure 6b).

©2014. American Geophysical Union. All Rights Reserved.

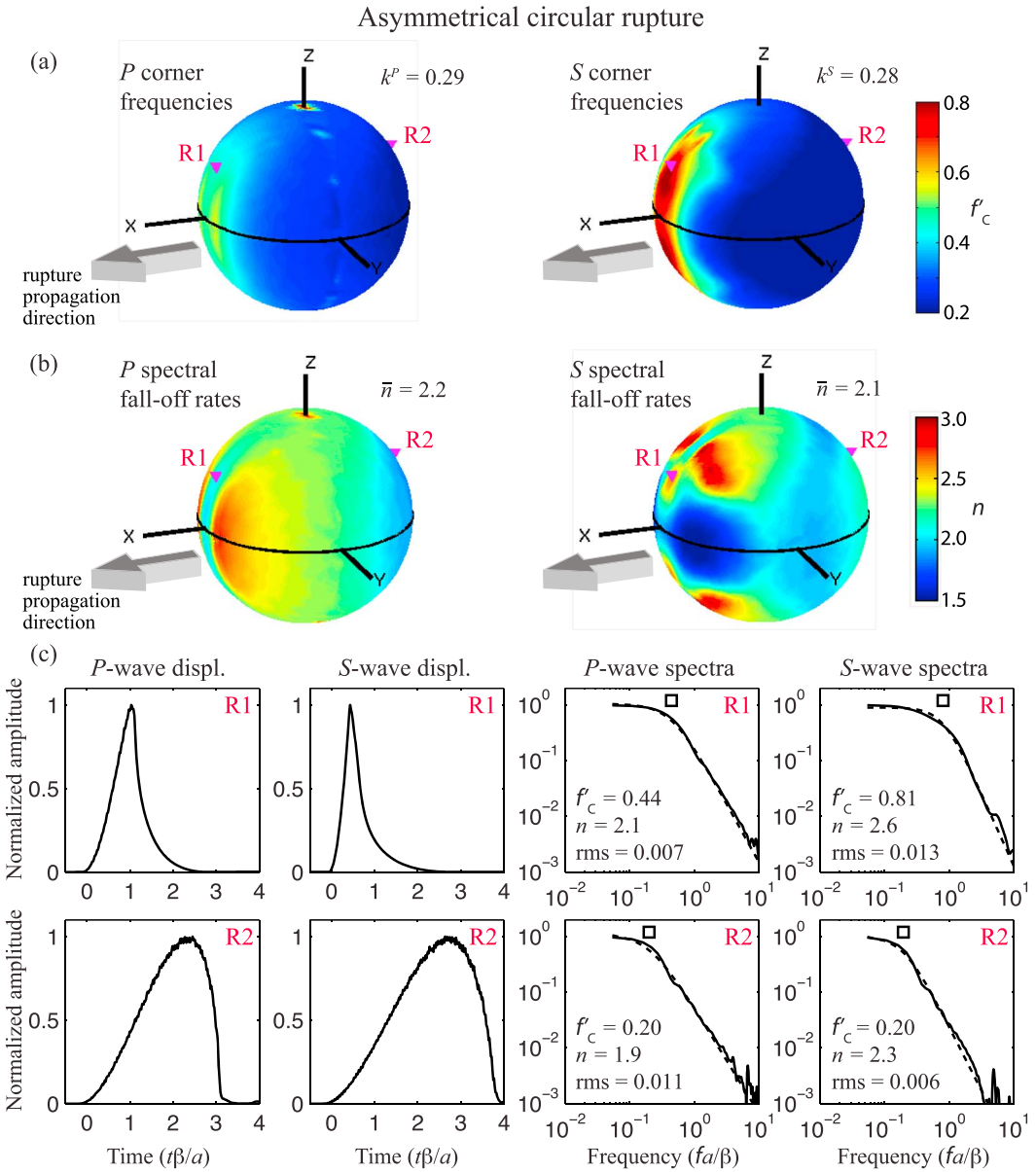

Figure 6. Far-field displacements, spectra, and corner frequencies f'_c for the asymmetrical circular model with rupture speed $V_r/\beta = 0.9$ shown in Figure 5. (a) Variations of f'_c over the focal sphere. The black circle on the *x*-*y* plane is parallel to the fault surface. The hypocenter is located in the R2 side. The values of k^P and k^S (i.e., the spherical average of f'_c) are indicated. (b) Variations of *P* and *S* spectral fall-off rates over the focal sphere. The spherical average of fall-off rates $\bar{n}$ is indicated. (c) Magnitude of far-field displacements and spectra at receivers R1 and R2. Dashed lines show the best fitting model of equation (17) with fall-off rate *n*, root-mean-square error (RMS), and corner frequency f'_c (open square).

The relations between the spherical average of *P* and *S* corner frequencies and the source radius are found as

$$\bar{f}_c^P = k^P \frac{\beta}{a} = 0.29\frac{\beta}{a} \tag{22}$$

$$\bar{f}_c^S = k^S \frac{\beta}{a} = 0.28\frac{\beta}{a} \tag{23}$$

for the asymmetrical circular model with the rupture speed $V_r = 0.9\beta$. The source duration of the asymmetrical model is longer, and hence, the durations of the displacement pulses are generally longer than those of the symmetrical model. This leads to smaller k^P. Interestingly, k^S for the asymmetrical model is slightly larger than that of the symmetrical model (compare equation (18) and equation (23)). Although

©2014. American Geophysical Union. All Rights Reserved.

the overall source duration is longer and hence the corner frequencies are generally smaller for the asymmetrical model, the strong directivity of *S* waves leads to larger corner frequencies locally (e.g., at receiver R1 in Figure 6), making the average value k^s comparable to that of the symmetrical source model.

The values of k, stress drop, scaled energy, and radiation efficiency for models with other subshear rupture speeds are shown in Table 1. The k values increase with the rupture speed and are generally smaller than those of the symmetrical model, consistent with the results of *Dong and Papageorgiou* [2002a]. Unlike the symmetrical models, the *P* and *S* wave normalized corner frequencies for the asymmetrical models are comparable and their ratio k^p/k^s remains roughly constant over a range of rupture speeds (Table 1). The stress drop increases slightly with the rupture speed V_r but generally remains almost independent of V_r (Table 1). The scaled energy E'_r/M'_0 and the radiation efficiency η_{eff} are generally smaller by a factor of 1.1 to 1.7 than those of the symmetrical model with the same rupture speed (Table 1). This is expected because the radiation efficiency depends on the effective source duration, which is longer in the asymmetrical models.

The ratios of *S*-to-*P* radiated energy E^s_r/E^p_r for the asymmetrical models are systematically larger than those of the symmetrical models (Table 1). For example, in the asymmetrical model with $V_r = 0.9\beta$, $E^s_r/E^p_r = 37$, which is 1.7 times larger than that of the symmetrical model. Since radiated energy is generally smaller for spectra with smaller corner frequencies, small k^p relative to k^s in the asymmetrical models leads to smaller E^p_r and hence larger E^s_r/E^p_r.

We have also computed a source scenario where the nucleation is at the bottom of the circular source, and hence, the rupture is predominantly Mode III (not shown in this work). In such a case, the patterns of corner frequencies and spectral fall-off rates with respect to the hypocentral location are quite similar to the asymmetrical source scenario discussed above.

5. Symmetrical Elliptical Rupture

We further consider elliptical source geometries where the rupture nucleates at the center of the ellipse and propagates at different speeds in different directions (Figure 1c). In what we call "symmetrical elliptical models," we construct the source geometry such that the rupture front simultaneously reaches the periphery of the elliptical region with the major and minor axes a and b, respectively. Mathematically, this means that

$$\frac{V_x}{V_y} = \frac{a}{b}, \tag{24}$$

and the stopping phases are generated at that same instance once the rupture reaches the edge of the elliptical source. Using this source scenario, we explore the effects of subshear and supershear ruptures on the resulting corner frequencies and other source parameters.

Slip and stress drop distributions for a representative model are shown in Figure 7. The source behavior of symmetrical elliptical models is qualitatively similar to that of symmetrical circular ones. The amplitudes of slip and stress change in the circular and elliptical models are comparable (Figure 7). As in symmetrical circular models, the actual stress drop is up to 2 times larger than the dynamic stress drop $\Delta\sigma_d$ near the center of the fault, and the resulting fracture energy is smaller in the Mode II direction than the Mode III direction (Figure 7). Since the rupture speed in the Mode II direction is supershear in this model, the fracture energy in that direction is smaller than that of the circular source with $V_r = 0.9\beta$ shown in Figure 3e.

The corresponding far-field displacement pulses and their spectra are shown in Figure 8. For subshear rupture, the elliptical model shows a moderate azimuthal dependence of corner frequencies over the focal sphere due to the ellipticity of the source (Figure 8a). The direction of the major axis of the ellipse generally coincides with longer durations of the displacement pulses and hence smaller corner frequencies (e.g., receiver R1 in Figure 8a), because it takes a longer time for the stopping phases to sweep through the source region in that direction. The durations of displacement pulses are generally longer, and hence, f_c is smaller in the symmetrical elliptical model than the symmetrical circular model (compare Figure 4c and Figure 8b). Another notable difference is the scaled energy E'_r/M'_0. For a given rupture speed, E'_r/M'_0 and the radiation efficiency η_{eff} are smaller by up to a factor of 2 in the elliptical models than the circular models for the same rupture speed (Table 1), consistent with the results of *Dong and Papageorgiou* [2003]. Both E'_r/M'_0 and η_{eff} decrease with models with larger eccentricity ε, or a higher degree of ellipticity of the source.

For supershear rupture, the general pattern of the corner frequencies remains the same as that in the subshear rupture; however, the variability of both f^p_c and f^s_c over the focal sphere is greatly enhanced, with

©2014. American Geophysical Union. All Rights Reserved.

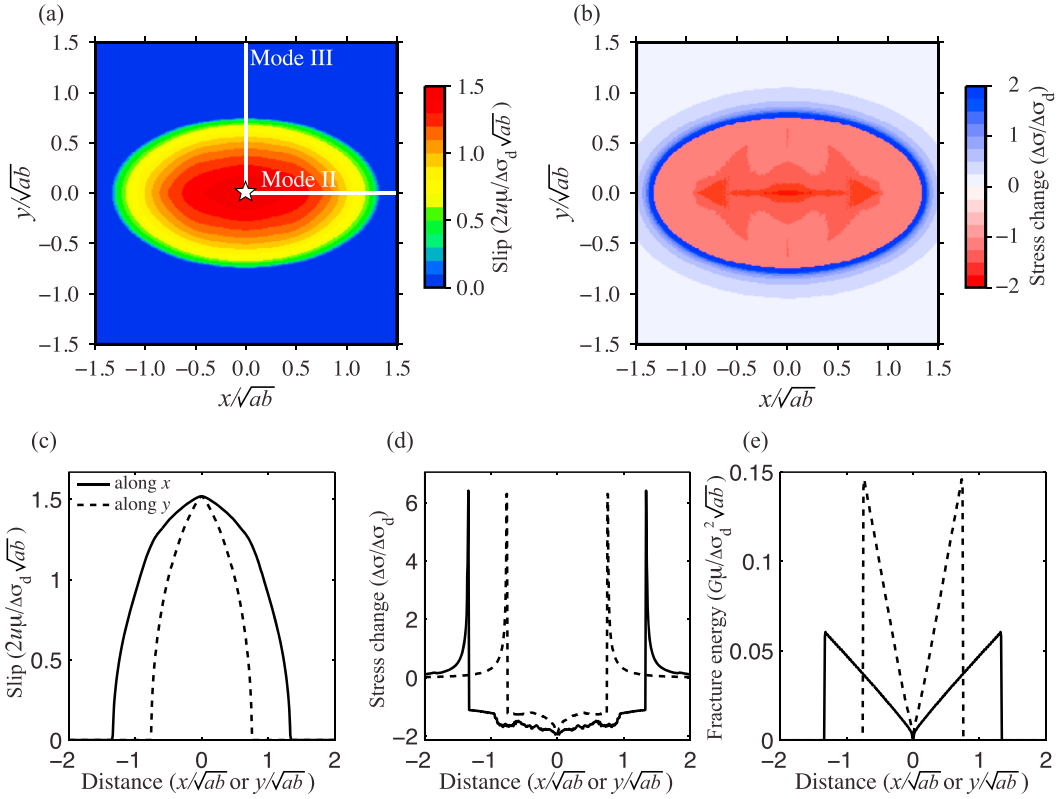

Figure 7. Characteristics of a symmetrical elliptical source with the rate of frictional weakening $A'_w = 84$, eccentricity $\varepsilon = 0.83$, rupture speeds $V_x/\beta = 1.6$, and $V_y/\beta = 0.9$. (a) Final slip distribution and (b) the corresponding stress-change distribution on the fault. White star indicates the hypocenter. (c–f) The profiles of slip S', stress change $\Delta\sigma'$, and fracture energy G' along the x (solid) and y (dashed) directions.

f_c^p and f_c^s ranging from 0.2 to 0.8 depending on the takeoff angles (Figure 8c). This enhanced variability is reflected by greater variability in durations of displacement pulses (Figure 8d). The relations between the spherical average of P and S corner frequencies and the source radius are found as

$$\bar{f}_c^p = k^p \frac{\beta}{\sqrt{ab}} = 0.42 \frac{\beta}{\sqrt{ab}} \tag{25}$$

$$\bar{f}_c^s = k^s \frac{\beta}{\sqrt{ab}} = 0.28 \frac{\beta}{\sqrt{ab}} \tag{26}$$

for the symmetrical elliptical model with the rupture speeds $V_x = 1.6\beta$ and $V_y = 0.9\beta$. The supershear rupture models result in shorter durations of the displacement pulses and hence larger normalized corner frequencies over the focal sphere than those in the subshear ones. The values of k^p and k^s generally increase with the rupture speed even in the supershear regime (Table 1). The scaled energy E'_r/M'_0 also increases with the rupture speed, as expected. The spherical average of the spectral fall-off rates $\bar{n}$ remains roughly the same over a wide range of rupture speeds, with $\bar{n}$ being 2.4 to 2.5 for P waves and 1.9 to 2.0 for S waves, which are similar to those in the symmetrical circular subshear ruptures. Hence, the general behavior of the spherical average of corner frequencies and other source parameters in the subshear regime extends to the supershear regime.

We calculate the stress drop using equation (A1), which takes into account the ellipticity of the source. The stress drop increases slightly with the rupture speed V_r but generally remains almost independent of V_r even in the supershear regime (Table 1).

6. Asymmetrical Elliptical Rupture

Lastly, we consider asymmetrical elliptical models where the rupture nucleates at one end and propagates mostly unilaterally at a subshear or supershear speed while maintaining the elliptical shape of the rupture

©2014. American Geophysical Union. All Rights Reserved.

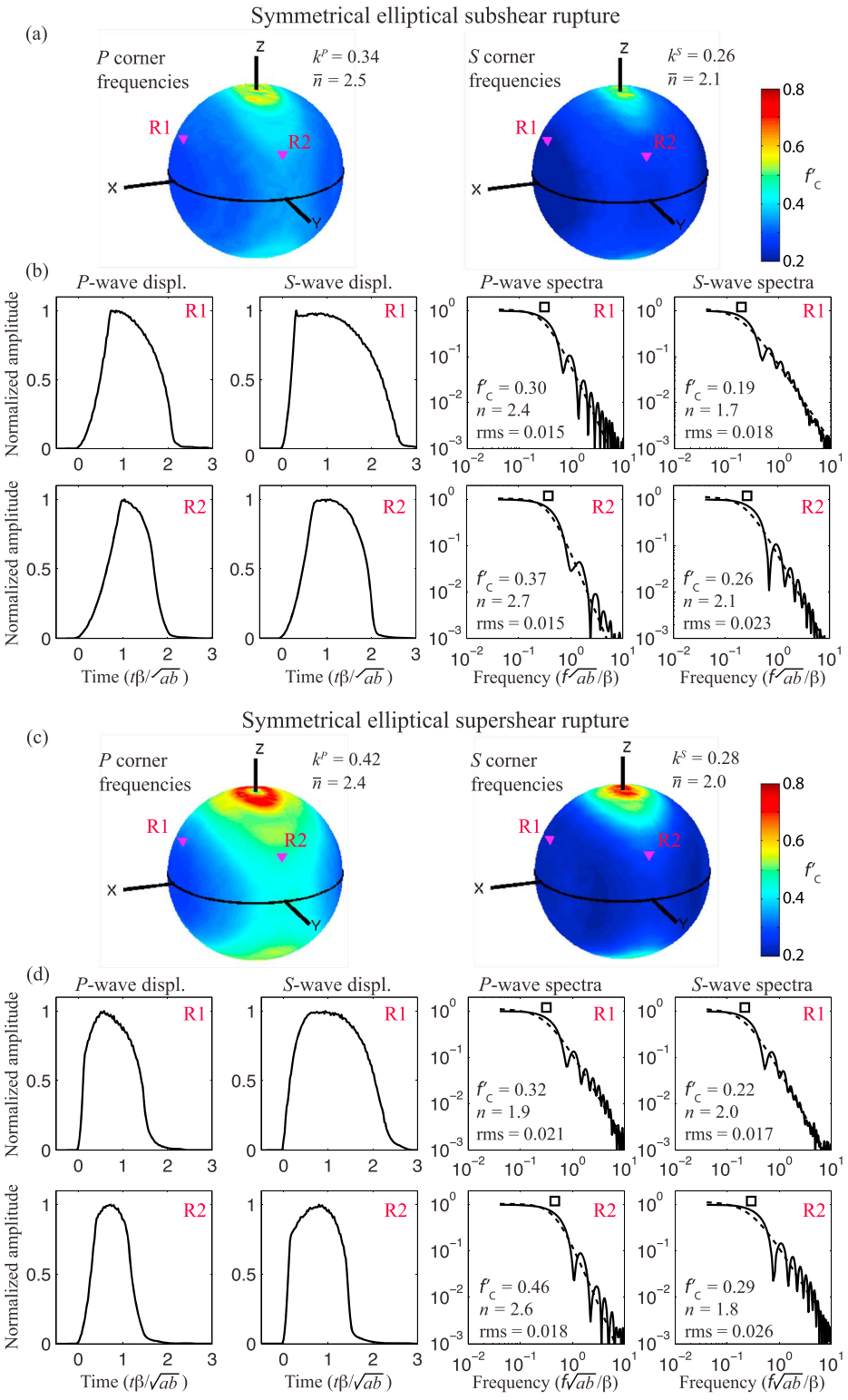

Figure 8. Far-field displacements, spectra, and corner frequencies f'_c for symmetrical elliptical models with subshear and supershear rupture speeds. (a) Variations of f'_c over the focal sphere for a model with eccentricity $\varepsilon = 0.83$, rupture speeds $V_x/\beta = 0.9$, and $V_y/\beta = 0.51$. The black circle on the *x*-*y* plane is parallel to the fault surface. The values of k^p and k^s (i.e., the spherical average of f'_c) and the average spectral fall-off rate $\bar{n}$ are indicated. (b) Magnitude of far-field displacements and spectra at receivers R1 and R2. Dashed lines show the best fitting model of equation (17) with fall-off rate *n*, root-mean-square error (RMS), and corner frequency f'_c (open square). (c–d) Similar plots for a model with eccentricity $\varepsilon = 0.83$, rupture speeds $V_x/\beta = 1.6$, and $V_y/\beta = 0.9$ shown in Figure 7.

©2014. American Geophysical Union. All Rights Reserved.

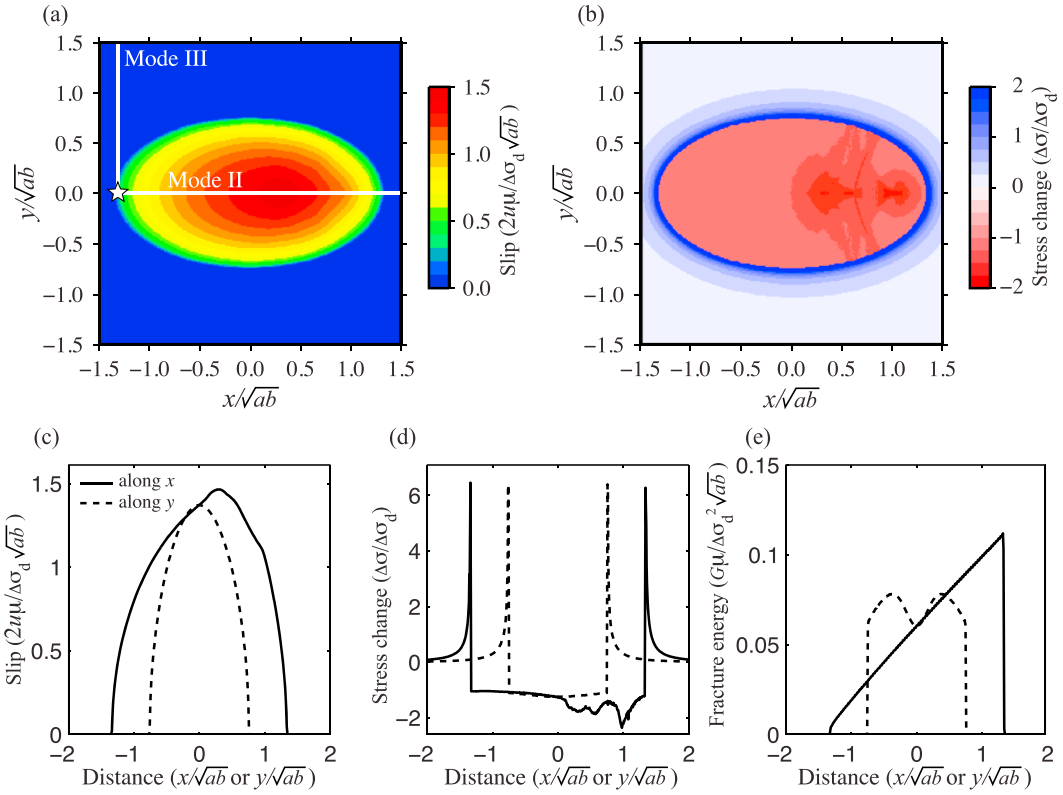

Figure 9. Characteristics of an asymmetrical elliptical source with the rate of frictional weakening $A'_w = 84$, eccentricity $\varepsilon = 0.83$, rupture speeds $V_x/\beta = 1.6$, and $V_y/\beta = 0.9$. (a) Final slip distribution and (b) the corresponding stress-change distribution on the fault. White star indicates the hypocenter. (c–f) The profiles of slip S', stress change $\Delta\sigma'$, and fracture energy G' along x (solid) and y (dashed) directions.

front (Figure 1d). As in the asymmetrical circular model, the stopping phases are continuously generated as the rupture front reaches the periphery of the source region. Despite the combined effect of rupture directivity and ellipticity of the source, the resulting slip, stress drop, and fracture energy distributions are qualitatively similar to those of the asymmetrical circular model, with comparable magnitude of slip and stress drop within the source region (compare Figure 5 and Figure 9).

The corresponding far-field displacements and corner frequencies show the greatest variability over the focal sphere among all the source scenarios we have considered (Figure 10). For example, for the model with supershear rupture shown in Figure 10c, f_c^p and f_c^s range from 0.18 to 1.3 and 0.15 to 0.90, respectively. As in the asymmetrical circular models, the rupture directivity enhances variability in the durations of the displacement pulses and hence their corner frequencies. The corner frequencies are larger at receivers located in the direction of rupture propagation (e.g., at receiver R1 in Figures 10a and 10b) than the region away from rupture propagation (e.g., at receiver R2). This directivity effect shows up in both subshear and supershear rupture regimes (Figures 10a and 10c).

The relations between the spherical average of P and S corner frequencies and the source radius are found as

$$\bar{f}_c^p = k^p \frac{\beta}{\sqrt{ab}} = 0.42\frac{\beta}{\sqrt{ab}} \tag{27}$$

$$\bar{f}_c^s = k^s \frac{\beta}{\sqrt{ab}} = 0.33\frac{\beta}{\sqrt{ab}} \tag{28}$$

for the asymmetrical elliptical model with the rupture speeds $V_x = 1.6\beta$ and $V_y = 0.9\beta$. Similar to the results for the circular source models, k^s is larger in the asymmetrical model than the symmetrical model (compare equation (26) and equation (28)). Although the overall source duration is longer and hence the corner frequencies are generally smaller for the asymmetrical model, the strong directivity leads to

©2014. American Geophysical Union. All Rights Reserved.

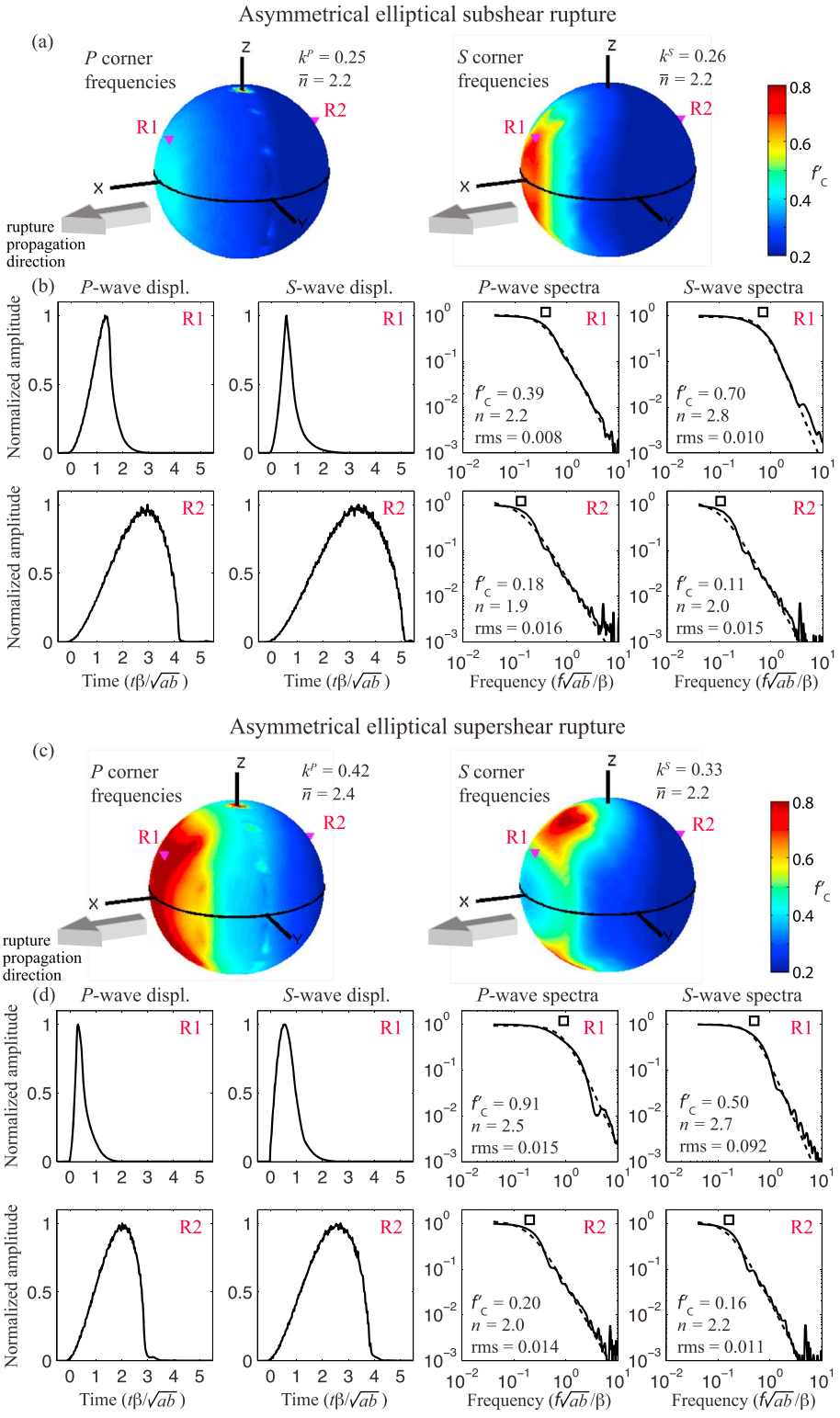

Figure 10. Far-field displacements, spectra, and corner frequencies f'_c for asymmetrical elliptical models with subshear and supershear rupture speeds. (a) Variations of f'_c over the focal sphere for a model with eccentricity $\varepsilon = 0.83$, rupture speeds $V_x/\beta = 0.9$, and $V_y/\beta = 0.51$. The black circle on the *x*-*y* plane is parallel to the fault surface. The hypocenter is located in the R2 side. The values of k^P and k^S (i.e., the spherical average of f'_c) and the average spectral fall-off rate $\bar{n}$ are indicated. (b) Magnitude of far-field displacements and spectra at receivers R1 and R2. Dashed lines show the best fitting model of equation (17) with fall-off rate *n*, root-mean-square error (RMS), and corner frequency f'_c (open square). (c–d) Similar plots for a model with eccentricity $\varepsilon = 0.83$, rupture speeds $V_x/\beta = 1.6$, and $V_y/\beta = 0.9$ shown in Figure 9.

©2014. American Geophysical Union. All Rights Reserved.

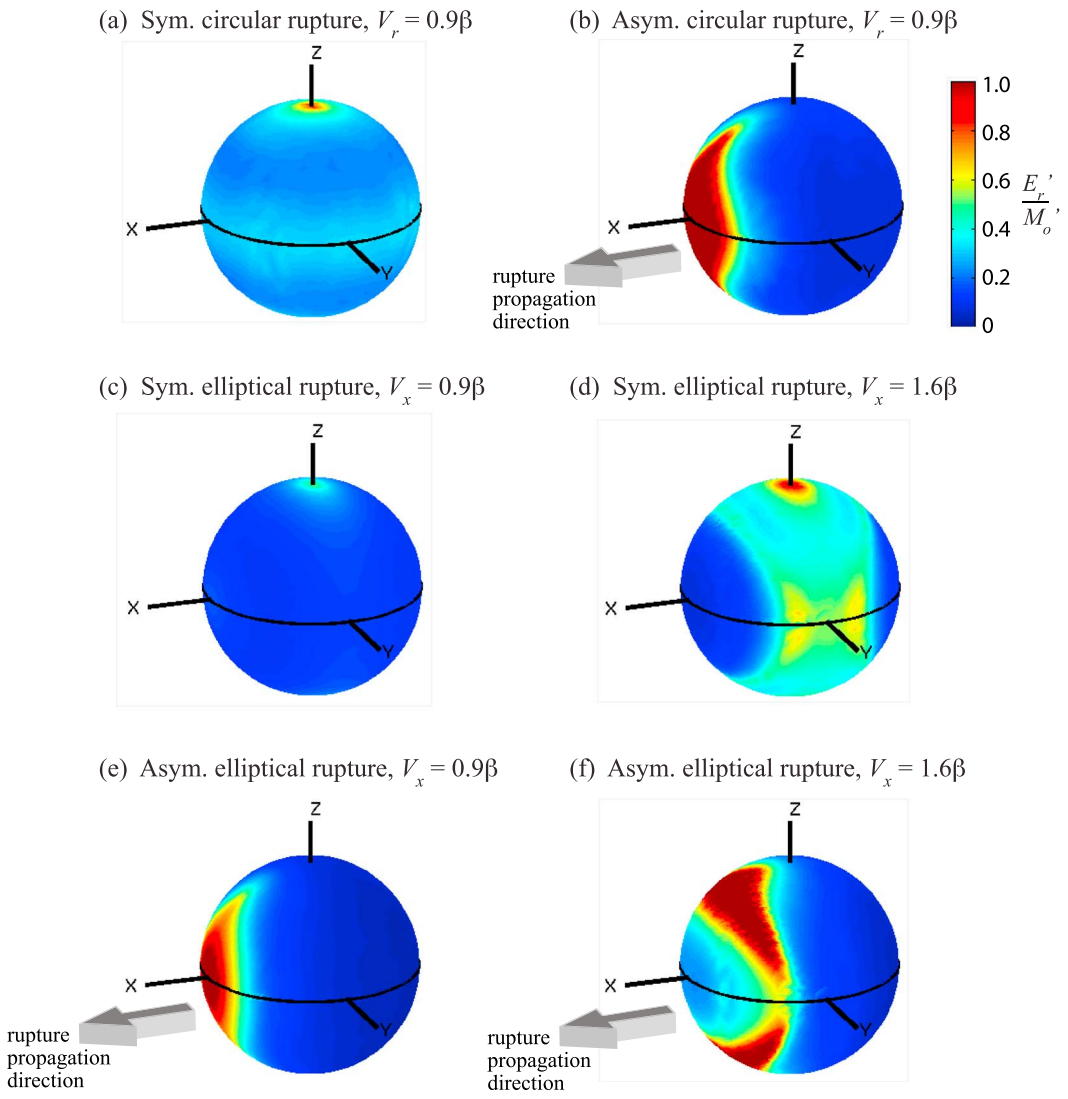

Figure 11. (a–f) Variations of S scaled energy $E_r'^s/M_0'$ over the focal sphere for different source scenarios. The scaled energy is calculated using a single-station estimation method discussed in the text.

larger corner frequencies locally, making the average value k^s larger than that of the symmetrical elliptical model (compare receiver R1 in Figure 8d and Figure 10d). As in the symmetrical elliptical source, the stress drop increases slightly with the rupture speed V_x but generally remains almost independent of V_x even in the supershear regime (Table 1). The scaled energy and radiation efficiency in both the symmetrical and asymmetrical elliptical models are similar despite different source durations and k values in those cases.

For supershear rupture, the P wave corner frequency is much larger than that of the subshear rupture, as the directivity effects become stronger when the rupture speed approaches the P wave speed (Figure 10c). In addition, the ascending segment of the S wave displacement pulses is convex upward at some takeoff angles where shear Mach waves are expected (e.g., receiver R1 in Figure 10d). Furthermore, the pattern of the S wave corner frequencies over the focal sphere is different from that of the subshear rupture (Figures 10a and 10c). These features are related to shear Mach waves produced by the propagation of supershear rupture. Indeed, the S wave corner frequencies are the largest at the "Mach angle" $\cos^{-1}(\beta/V_r)$ (= 51.3° in the case of Figure 10c) [e.g., *Bernard and Baumont*, 2005; *Mello et al.*, 2010]. These results suggest that earthquakes with subshear and supershear rupture speeds can be distinguished by analysis of variability in corner frequencies.

©2014. American Geophysical Union. All Rights Reserved.

Another notable difference between subshear and supershear ruptures is that k^p and k^s for supershear ruptures are no longer similar, and the k^p/k^s ratio increases with the rupture speed (Table 1). This is also reflected by the ratio of *S*-to-*P* radiated energy E_r^s/E_r^p, which increases with the rupture speed in the subshear regime, whereas E_r^s/E_r^p decreases with increasing rupture speed in the supershear regime, with the smallest $E_r^s/E_r^p = 12$ obtained for $V_x = 1.6\beta$ (Table 1). Since radiated energy is generally larger for spectra with larger corner frequencies, large k^p relative to k^s in the supershear regime leads to large E_r^p and hence small E_r^s/E_r^p.

7. Estimation of Radiated Energy

The radiated energy of an earthquake is often estimated from far-field spectra on a station-by-station basis. We quantify variability in estimated radiated energy using computed far-field spectra for the source models considered in this work. In a uniform whole space, the far-field radiated *S* wave energy may be expressed as

$$E_r^s = \frac{\langle \Psi_s^2 \rangle}{4\pi\rho\beta^5} M_0^2 \int_0^\infty |\omega A(\omega)|^2 \mathrm{d}\omega \,, \tag{29}$$

where $\langle \Psi_s^2 \rangle$ is the mean over the focal sphere of the radiation pattern Ψ_s^2 (=2/5 for *S* waves), M_0 is the seismic moment, ω is the angular frequency, and $A(\omega)$ is the normalized displacement spectrum [*Mayeda and Walter*, 1996; *Baltay et al.*, 2011]. This single-station estimate is corrected for the radiation pattern but can still be biased by directivity effects. The nondimensional scaled energy may be expressed as

$$\frac{E_r'^s}{M_0'} = \frac{E_r^s}{M_0}\frac{\mu}{\Delta\sigma_d} = \frac{\langle \Psi_s^2 \rangle}{4\pi\beta^3\Delta\sigma_d} M_0 \int_0^\infty |\omega A(\omega)|^2 \mathrm{d}\omega \,. \tag{30}$$

Figure 11 shows the variations of estimated scaled energy $E_r'^s/M_0'$ over the focal sphere for different source scenarios. Since *S* wave radiated energy is much larger than the *P* wave energy (i.e., $E_r^s \gg E_r^p$), the total scaled energy $E_r/M_0 \approx E_r^s/M_0$. For symmetrical circular and elliptical models, the estimated scaled energy does not vary much over the focal sphere, although the supershear rupture scenario shows a moderate azimuthal dependence (Figures 11a, 11c, and 11d). On the other hand, the asymmetrical circular and elliptical models show large variations in the estimated scaled energy over the focal sphere (Figures 11b, 11e, and 11f). For example, in the asymmetrical elliptical rupture with $V_x = 1.6\beta$, $E_r'^s/M_0'$ ranges from 0.04 to 4.0 depending on the takeoff angle. Due to the directivity effects, the scaled energy is much larger at receivers located in the direction of rupture propagation than the region from which the rupture propagates away. The patterns of estimated radiated energy and corner frequencies are quite similar, and the regions of larger radiated energy coincide with those of larger corner frequencies and vice versa (compare Figure 6a and Figure 11b). For the asymmetrical elliptical supershear rupture, locally large $E_r'^s/M_0'$ is associated with shear Mach waves emerged at the "Mach angle" $\cos^{-1}(\beta/V_r)$ (Figures 11f). We discuss uncertainty in radiated energy estimates due to limited station coverage in section 8.

8. Discussion

8.1. Dependence of Corner Frequencies on Rupture Speeds

We compare the dependence of normalized corner frequencies k^p and k^s on the rupture speed V_r for all the models considered in this work (Figure 12). For a given source geometry and rupture style, the relation between k^p and V_r is almost linear over the range of rupture speeds (Figure 12a). On the contrary, the dependence of k^s on V_r shows more complex behavior, although k^s is still a monotonic function of V_r for a given source geometry and rupture style (Figure 12b).

8.2. Implications for Variability in Stress Drops and Radiation Efficiency in Observational Work

Stress drop estimates over wide regions are observed to exhibit large scatter, with variations on the order of 10^2 even for events recorded by 20 or more stations [e.g., *Shearer et al.*, 2006]. This scatter is reduced somewhat for nearby earthquakes, but stress drops for closely spaced events still vary by factors of 20 or more. A key question is how much of this scatter is caused by variability of source parameters that are independent of the actual stress drop. For the corner frequencies reported in Table 1 and Figure 12, we find that k_p and k_s range from 0.19 to 0.42 and 0.19 to 0.33, respectively, despite similar static stress drops $\Delta\sigma$ among different source scenarios. This means that, by assuming k in equation (4) derived from a particular model (e.g., the symmetrical circular rupture with $V_r = 0.9\beta$), estimated stress drops for these events would

©2014. American Geophysical Union. All Rights Reserved.

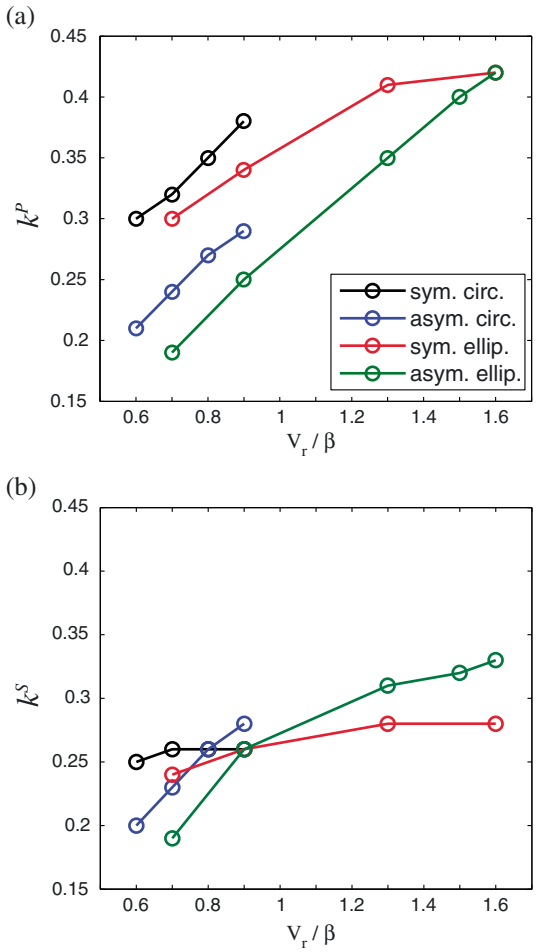

Figure 12. (a and b) Dependence of spherical average of normalized corner frequencies k^P and k^S on the rupture speed V_r for all the source scenarios.

vary by a factor of 5–10 depending on the differences in source geometry, rupture styles, and rupture speeds. This variability is likely to be small compared to that in real earthquakes, given that the source geometry and rupture styles considered here are still relatively simple.

Additional source complexity can further affect k_p, k_s, and resulting stress drop estimates. Our source models are characterized by constant rupture speeds, regular source geometry (i.e., circular or elliptical), and near-uniform stress drops. It is likely that real earthquakes, even small, are not that regular. By considering singular crack solutions with instantaneous fault healing, *Dong and Papageorgiou* [2002b] found that variable rupture speeds can enhance directivity effects with stronger radiation channeled in the direction of crack growth. Their results indicate that, with accelerating or decelerating rupture, variability in corner frequencies over the focal sphere can increase further and influence k_p and k_s. In addition, *Noda et al.* [2013] argued that the spatial average of heterogeneous stress drop can differ from the moment-based stress drop (equation (2)) by up to a factor of 2. Quantifying the relative importance of these complexities will be needed to understand the large uncertainties in stress drop estimates.

Since source geometry and rupture speed for small earthquakes are generally unknown, one can explain an anomalously low corner frequency with either a small stress drop or a slower rupture speed. This trade-off propagates through radiation efficiency estimates. To quantify the uncertainty in radiation efficiency associated with unknown source geometry and rupture speed, we estimate radiation efficiency $\eta_{\text{eff}} = 2\mu E_r/(\Delta\sigma M_0)$ for all the source models assuming that the sources are symmetrical circular ruptures with speed $V_r = 0.9\beta$. Figure 13 compares these estimated radiation efficiencies (dashed lines) computed from both *P* and *S* wave stress drop estimates to the true radiation efficiencies (solid lines), as a function of rupture geometry and speed. In general, the true radiation efficiency increases with rupture speed and is also somewhat higher for the circular crack models compared to the elliptical models. However, when the actual rupture speed is smaller than the assumed 0.9β, the stress drop is underestimated and, as a result, the radiation efficiency η_{eff} is overestimated, often by factors of 2 or more. Large errors in estimated η_{eff} also occur when the wrong source geometry or rupture directivity is assumed. The bias is usually higher for η_{eff} estimates derived from *P* waves compared to *S* wave estimates because k^P exhibits larger variations than k^S (see Table 1). These biasing effects indicate that radiation efficiency estimates derived from observed seismic spectra should not be directly interpreted as describing rupture properties unless there are independent constraints on rupture speed and geometry. In particular, analysis of a low rupture speed earthquake may not yield the expected low-radiation efficiency estimate if the estimate is obtained from a model that assumes a higher rupture speed.

8.3. Uncertainty in Corner Frequency Estimation due to Limited Station Coverage

An underappreciated aspect of the Madariaga model, confirmed by our own work, is the large dependence of f_c on takeoff angle relative to the source, which is greatly enhanced by the directivity effect (e.g., Figure 6a). Thus, measurements from a small number of seismic stations are unlikely to produce unbiased estimates of spherically averaged f_c, even if we assume that attenuation corrections are perfect.

©2014. American Geophysical Union. All Rights Reserved.

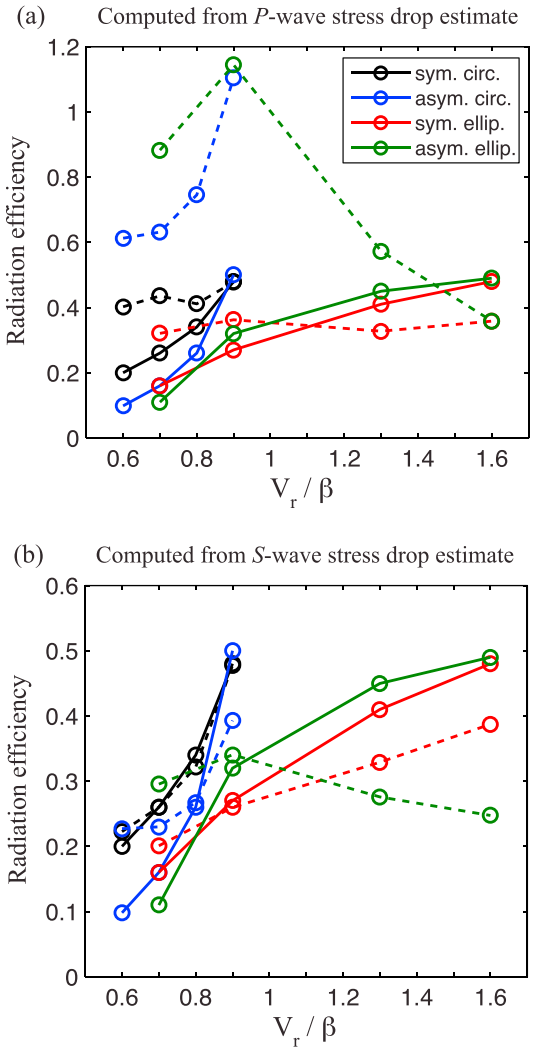

Figure 13. Errors in estimated radiation efficiency due to unknown source geometry and rupture speed, for stress drop estimates obtained from (a) *P* waves and (b) S waves. Solid lines plot the "true" radiation efficiency of each source model η^{rad}_{true} as a function of rupture speed. For comparison, the dashed lines show estimated radiation efficiency $\eta^{rad}_{estimated} = 2\mu E_r/(\Delta\sigma M_0)$ computed by assuming the correct E_r/M_0 and the spherical average of corner frequencies $\bar{f}_c$, the relation between $\Delta\sigma$ and $\bar{f}_c$ for a circular source (equation (4)), and a single fixed value of k^P or k^S obtained from the symmetrical circular rupture with $V_r = 0.9\beta$. Note that when the rupture speed is actually smaller than the 0.9β used for the estimation, one will obtain incorrectly higher radiation efficiency.

A factor of 2 difference in the spherical average of corner frequencies $\bar{f}_c$ will produce a factor of 8 difference in stress drop. As an example, synthetic tests of random takeoff angles show large scatter in stress drop estimates from single-station measurements, which is reduced as more stations are averaged (see Figure 14). Histograms of $\log_{10}\Delta\sigma$ estimates in Figure 14 are approximately lognormal distributed, and standard errors in $\log_{10}$ stress drops are 0.34 and 0.55 for single-station *P* and *S* wave estimates, respectively, which are reduced to 0.17 and 0.30 for five-station estimates and 0.12 and 0.21 for ten-station estimates. Note that, for example, ± 0.55 in $\log_{10}\Delta\sigma$ gives standard error bars that span from 0.29 to 3.5 times the true stress drop; that is, there is a 68% chance the true stress drop is within that range. These should be taken as lower bounds on the errors because it is unlikely that the true station distribution will mimic random takeoff angles.

8.4. Uncertainty in Radiated Energy Estimation due to Limited Station Coverage

Using the estimated scaled energy described in section 7, we quantify uncertainty in scaled energy estimates due to limited station coverage. Figure 15 shows histograms of normalized scaled energy estimates for three source scenarios in Figure 11. As expected, standard errors in $\log_{10}(E_r/M_0)$ are quite small for symmetrical models (e.g., Figure 15a). However, for asymmetrical models, the standard errors increase significantly due to the directivity effects. For example, the standard error in $\log_{10}(E_r/M_0)$ for the asymmetrical circular model is 0.39 for single-station estimates, which is reduced to 0.27 for five-station estimates and 0.20 for ten-station estimates (Figure 15b). The standard errors are even larger for the asymmetrical elliptical supershear rupture (Figure 15c). Hence, as in stress drop estimates, the large dependence of scaled energy on takeoff angle relative to the source suggests that measurements from a small number of seismic stations are unlikely to produce unbiased estimates of spherically averaged scaled energy.

Given a limited number of stations available for seismic observations, what kind of station coverage is optimal for estimating corner frequencies and scaled energy? Our results show that the patterns of corner frequencies and scaled energy over the focal sphere depend on source geometry, rupture directivity, and rupture speeds (e.g., Figure 11). This suggests that an approximately uniform coverage of seismic stations over the focal sphere will most accurately capture the spherical average of these parameters. Utilizing seismic stations covering only one side of the focal sphere (e.g., on-land seismometers recording offshore events in subduction zones) likely increases the bias in estimating the spherical average.

8.5. Uncertainty in Radiation Efficiency Estimation due to Limited Station Coverage

We further quantify uncertainty in radiation efficiency estimates for a few selected source scenarios (Figure 16). We calculate radiation efficiency η_{eff} from single-station estimates of scaled energy E'_r/M'_0

©2014. American Geophysical Union. All Rights Reserved.

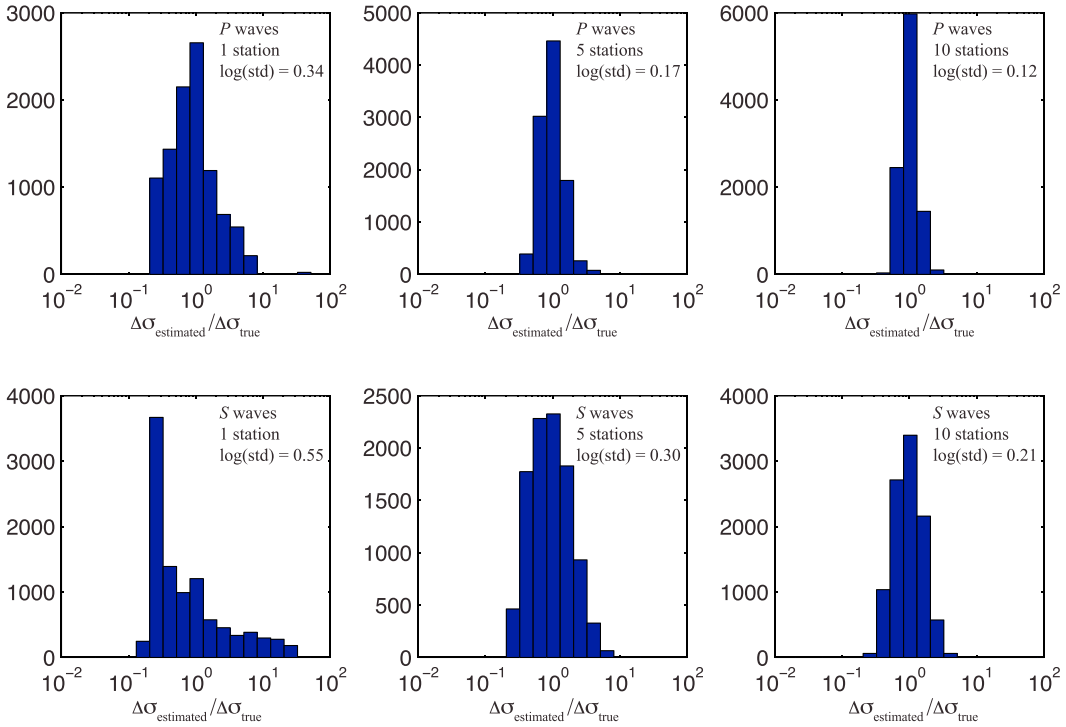

Figure 14. Histograms of normalized stress drops for different numbers of random stations based on the corner frequencies shown in Figure 6a. The horizontal axis shows estimated stress drop $\Delta\sigma_{estimated}$ normalized by the true stress drop $\Delta\sigma_{true}$ obtained from perfect station coverage. The standard deviation (std) in $\log_{10}\Delta\sigma_{estimated}$ and the number of stations are indicated in each panel.

and *S* wave corner frequencies (and stress drops $\Delta\sigma$). We find that standard errors in $\log_{10}\eta_{eff}$ are larger than those of the scaled energy for the symmetrical circular models (Figure 16a). This is expected because radiation efficiency depends on the ratio of scaled energy to stress drop and hence is affected by errors in either parameter. On the other hand, the standard errors in radiation efficiency for the asymmetrical models are smaller than those in scaled energy. For example, the standard error in $\log_{10}\eta_{eff}$ for the asymmetrical circular model is 0.25 for single-station estimate, whereas that in $\log_{10}(E_r/M_0)$ is 0.39 (Figures 15b and 16b). Since the regions of larger scaled energy coincide with those of larger corner frequencies (and the stress drops), the radiation efficiency, which is the ratio of these quantities, cancels out the directivity effect to some degree.

8.6. On Averaging of Corner Frequencies From Individual Spectra Versus From Stacked Spectra

Uncertainty in stress drop estimation also includes how the average of corner frequencies $\bar{f}_c$ is calculated. In this work, we follow the approach of *Madariaga* [1976] where $\bar{f}_c$ is the average of all the f_c estimated for individual spectra. At the same time, observational studies [e.g., *Prieto et al.*, 2004; *Shearer et al.*, 2006] often use stacked log spectra in fitting a spectral function (e.g., equation (17)) because individual spectra tend to be irregular in shape and difficult to fit robustly. Figures 17a and 17b show log spectra, their average (stack), and the corresponding estimated corner frequencies *k* for the source model shown in Figure 5. The values of k^p and k^s differ from those estimated from the spherical average by 3% in this case. When estimating f_c from the stacked spectra for all the source scenarios, the standard errors of the difference between these two methods are 3 and 6% for k^p and k^s, respectively (Table 1). Hence, corner frequencies estimated by stacked spectra generally agree reasonably well with those of the spherical average.

Observational studies often also assume a fixed fall-off rate $n = 2$ in fitting spectra. With a fixed fall-off rate $n = 2$, k^p decreases from 0.30 to 0.26, whereas k^s increases from 0.27 to 0.30 (Figures 17c and 17d). Clearly, there is a trade-off between f_c and n in fitting the spectral function (17). For example, forcing n to be smaller than the actual fall-off rate leads to a smaller f_c, and this bias appears as a difference between the solid red and dashed red curves in Figure 17c. To understand how this assumption affects the resulting f_c, we estimate k^p and k^s by fitting with $n = 2$ to stacked spectra for all the source scenarios (Table 1). The resulting k^p and

©2014. American Geophysical Union. All Rights Reserved.

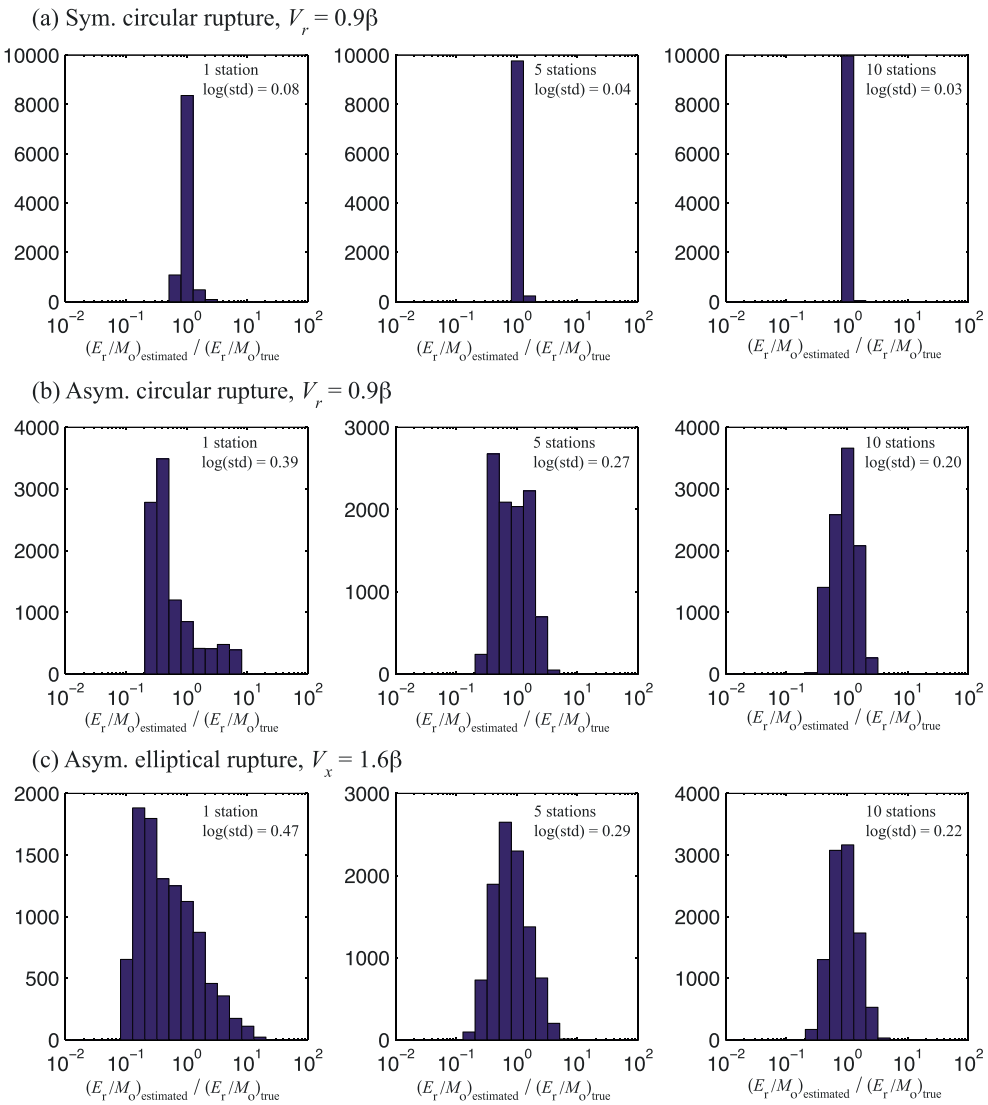

Figure 15. Histograms of normalized scaled energy for different numbers of random stations based on the corner frequencies for (a) the symmetrical circular model with $V_r = 0.9\beta$, (b) the asymmetrical circular model with $V_r = 0.9\beta$, and (c) the asymmetrical elliptical model with $V_x = 1.6\beta$. The horizontal axis shows estimated scaled energy $(E_r^s/M_0)_{estimated}$ normalized by the true scaled energy $(E_r/M_0)_{true}$ obtained from perfect station coverage. Both the radiated energy and seismic moment are estimated using an *S* wave spectrum at each station over the focal sphere. The standard deviation (std) in $\log_{10}(E_r^s/M_0)_{estimated}$ and the number of stations are indicated in each panel.

k^s are quite different and often smaller than those obtained with variable *n*. Interestingly, *k* values for the different assumed models agree better when the spectra are fit with $n = 2$ (Table 1).

8.7. On Using Objective Definitions of Corner Frequencies

Instead of fitting a function to a far-field displacement spectrum in estimating the corner frequency f_c, several possibly more objective definitions of f_c have been proposed in the literature. The corner frequency according to *Silver* [1983] is defined as

$$f_c^{Silver} = \frac{\sqrt{2}}{2\pi}\frac{1}{T}, \tag{31}$$

where T^2 corresponds to both the curvature of a displacement spectrum at zero frequency and the variance of the time domain pulse.

©2014. American Geophysical Union. All Rights Reserved.

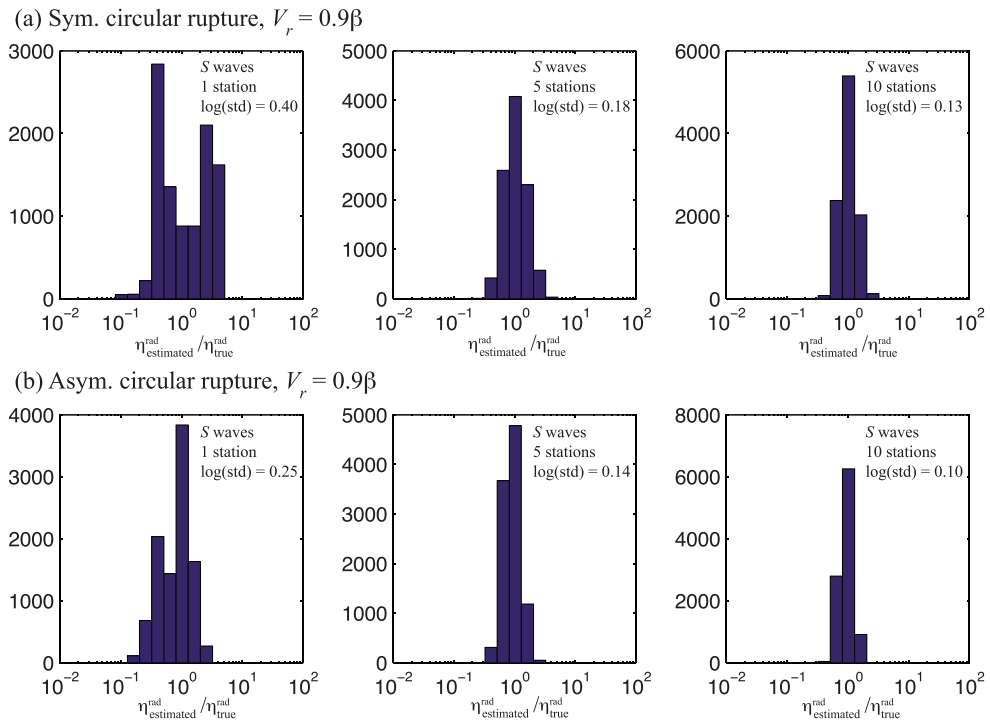

Figure 16. Histograms of normalized radiation efficiency for different numbers of random stations based on the corner frequencies for (a) the symmetrical circular model with $V_r = 0.9\beta$ and (b) the asymmetrical circular model with $V_r = 0.9\beta$. The horizontal axis shows estimated radiation efficiency $\eta^{rad}_{estimated} = 2\mu E^s_r/(M_0\Delta\sigma)$ normalized by the true radiation efficiency η^{rad}_{true} obtained from perfect station coverage. The radiated energy, seismic moment, and stress drop are estimated using a *S* wave spectrum at each station over the focal sphere. The standard deviation (std) in $\log_{10}\eta^{rad}_{estimated}$ and the number of stations are indicated in each panel.

The corner frequency according to *Snoke* [1987] is defined as

$$f_c^{Snoke} = \left[\frac{J}{2\pi^3\Omega_0^2}\right]^{1/3}, \tag{32}$$

where Ω_0 is the long-period spectral level and J is the second moment of the power spectrum given by

$$J = 2\int_0^\infty |\omega u(\omega)|^2 df = \frac{2}{3}[\Omega_0\omega_1]^2 f_1 + 2\int_{f_1}^{f_2} |\omega u(\omega)|^2 df + 2|\omega_2 u(\omega_2)|^2 f_2 \tag{33}$$

for the spectral bandwidth between f_1 and f_2. The method of *Snoke* [1987] was derived by assuming that the displacement spectrum has a fall-off rate $n = 2$ (i.e., the ω^2 model) at frequencies beyond f_2.

The corner frequency according to *Andrews* [1986] is defined as

$$f_c^{Andrews} = \left[\frac{J}{(2\pi)^2 K}\right]^{1/2}. \tag{34}$$

where

$$K = 2\int_0^\infty |u(\omega)|^2 df = 2[u(\omega_1)]^2 f_1 + 2\int_{f_1}^{f_2} |u(\omega)|^2 df + \frac{2}{3}|u(\omega_2)|^2 f_2\,. \tag{35}$$

Silver's definition is difficult to apply for real data as it measures the curvature of the spectrum at zero frequency, where the spectrum is typically not well resolved. In addition, *Dong and Papageorgiou* [2002a] concluded that the Silver method yields substantially larger values of f_c than other methods. We calculate

©2014. American Geophysical Union. All Rights Reserved.

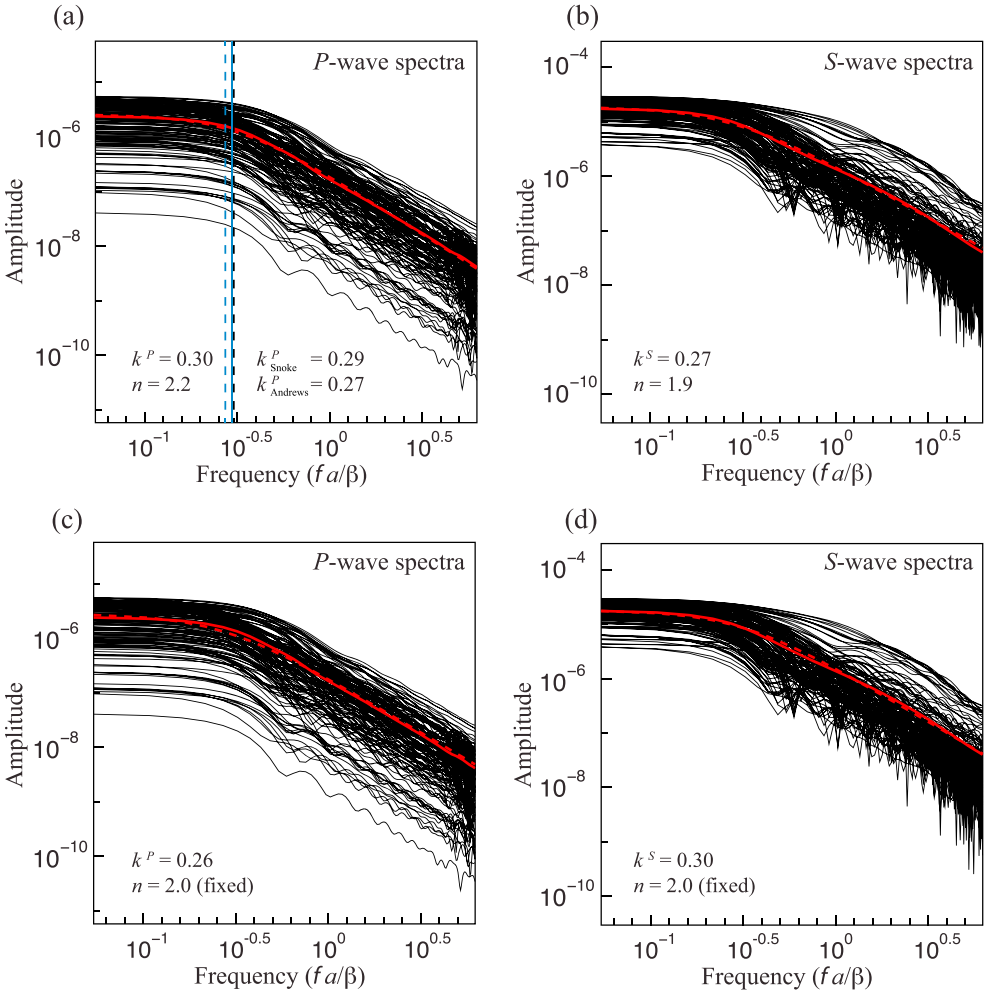

Figure 17. Individual spectra (black lines) at different takeoff angles for the source model shown in Figure 5. A fraction of all the spectra are plotted for (a) *P* and (b) *S* waves. The solid red line shows the average of the log spectra, and the corresponding best fitting spectral function (equation (17)) is shown by the dashed red line. The estimated corner frequencies, k^p and k^s, and fall-off rates *n* are indicated. Corner frequencies estimated from fitting the spectral function (dashed black line) and using the methods of Snoke (blue) and Andrews (dashed blue) are shown. (c–d) The same as Figures 17a and 17b except that the dashed red line is the best fitting spectral function with a fixed fall-off rate *n* = 2.0.

f_c^{Snoke} and f_c^{Andrews} using the far-field spectra for symmetrical and asymmetrical source models (Figure 18). Since both the Snoke and Andrews methods depend on the integral of the square of the velocity, the variations of the corner frequencies over the focal sphere resemble that of the scaled energy (e.g., compare Figures 18b, 18c, and 11b). We also find that the Snoke method provides the best estimate of the intersection of the low- and high-frequency asymptotes, whereas the Andrews method systematically yields lower f_c values (e.g., Figure 17a), consistent with the conclusion of *Dong and Papageorgiou* [2002a]. Furthermore, for all the symmetrical source models, the Snoke method is less dependent on the takeoff angle than is the spectral-fitting method (e.g., compare Figure 4a and Figure 18a).

For the Snoke method, the relations between the spherical average of *P* and *S* corner frequencies and the source radius are found as

$$\bar{f}_c^p = k^p_{\text{Snoke}} \frac{\beta}{a} = 0.38 \frac{\beta}{a} \tag{36}$$

$$\bar{f}_c^s = k^s_{\text{Snoke}} \frac{\beta}{a} = 0.36 \frac{\beta}{a} \tag{37}$$

©2014. American Geophysical Union. All Rights Reserved.

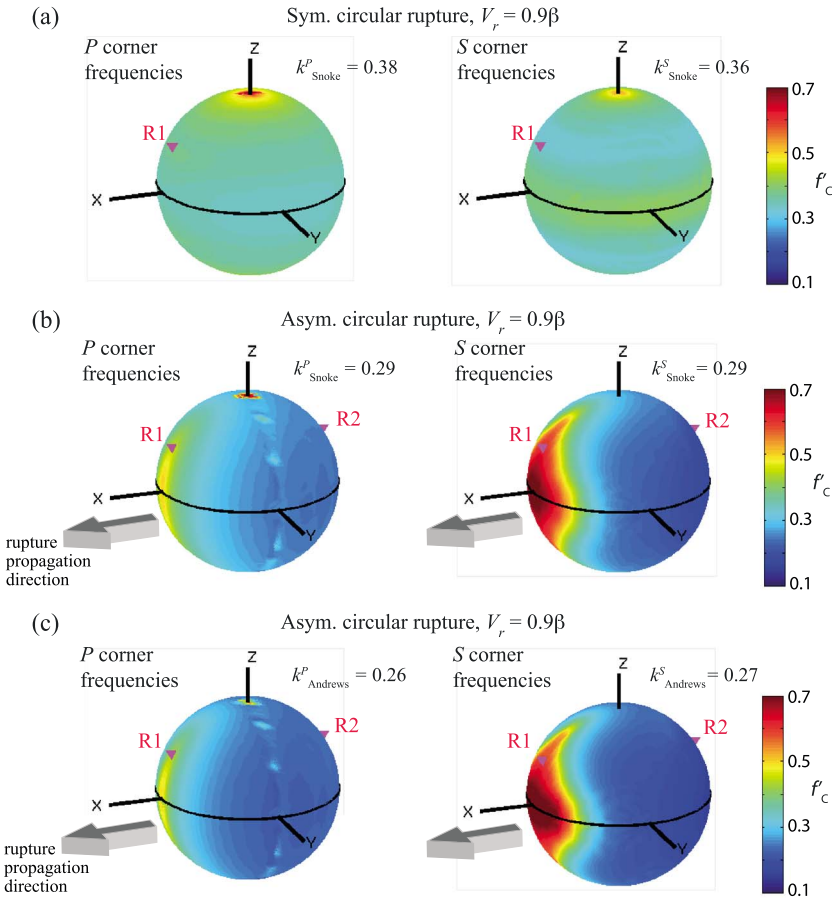

Figure 18. Variations of *P* and *S* corner frequencies calculated using the objective definition of *Snoke* [1987] for (a) the symmetrical circular model with $V_r = 0.9\beta$ and (b) the asymmetrical circular model with $V_r = 0.9\beta$. (c) The same as Figure 18b, but the corner frequencies are calculated using the objective definition of *Andrews* [1986]. The patterns of f_c over the focal sphere for the Snoke and Andrews methods are similar, although the Andrews method yields systematically smaller f_c.

for the symmetrical circular source with the rupture speed $V_r = 0.9\beta$. The equivalent relations for the asymmetrical circular source with the rupture speed $V_r = 0.9\beta$ are found as

$$\bar{f}^p_c = k^p_{Snoke}\frac{\beta}{a} = 0.29\frac{\beta}{a} \tag{38}$$

$$\bar{f}^s_c = k^s_{Snoke}\frac{\beta}{a} = 0.29\frac{\beta}{a}\,. \tag{39}$$

The values of k^p_{Snoke} and k^s_{Snoke} for all the source models reported in Table 1 agree well with k^p and k^s estimated by the spectral-fitting method, despite that the fact that the fall-off rates vary over the focal sphere and do not generally satisfy $n = 2$ as assumed in the Snoke method (e.g., Figure 6b). As *Snoke* [1987] originally argued, the Snoke method provides a relatively robust way to estimate the stress drop $\Delta\sigma$, given that $\Delta\sigma$ is proportional to $\Omega_0 k^3_{Snoke} = J/\Omega_0$ instead of $\Omega_0 k^3$ and that f^p_{Snoke} and f^s_{Snoke} are less dependent on the takeoff angle. However, since the Snoke or Andrews methods are related to radiated energy (J in equation (33)), one does not have separate estimates of stress drop and radiated energy to compute radiation efficiency, implying a constant value of radiation efficiency among different earthquakes when their source geometries and rupture speeds are unknown. Note also that there may be the problem of inadequate bandwidth in applying the Snoke method to real data.

9. Conclusions

Using simulations of dynamic rupture and the seismic representation theorem, we have computed far-field body wave spectra derived from source models with different source geometries, rupture directivity,

©2014. American Geophysical Union. All Rights Reserved.

and rupture speeds. For each source scenario, the characteristics of displacement spectra, their corner frequencies, scaled energy, and other source parameters have been reported. Compared to the symmetrical circular models of *Kaneko and Shearer* [2014], the asymmetrical models show (i) a stronger azimuthal dependence due to the asymmetry of the rupture evolution, resulting in much larger variability of estimated corner frequencies and scaled energy over the focal sphere, (ii) generally smaller values of spherical averages of *P* and *S* wave normalized corner frequencies k^p and k^s, (iii) a roughly constant ratio k^p/k^s over a range of rupture speeds, and (iv) a larger ratio of *S*-to-*P* radiated energy.

We have further explored the effects of supershear rupture on the resulting corner frequencies using elliptical source models. Symmetrical elliptical models exhibit an asymmetry of corner frequencies over the focal sphere due to the ellipticity of the source, which is greatly enhanced in models with a supershear rupture speed. Models with a faster rupture speed result in shorter durations of the displacement pulses and hence larger corner frequencies. The spherical average of the spectral fall-off rates remains roughly the same over a wide range of rupture speeds. Overall, the general behavior of the spherical average of corner frequencies in the subshear regime extends to the supershear regime.

However, there are differences in corner frequencies, scaled energy, and other source parameters for subshear and supershear ruptures, which are pronounced by directivity effects. Far-field displacements and spectra at some azimuth are influenced by shear Mach waves generated by the propagation of supershear rupture, resulting in different characteristics of the displacement pulses and patterns of corner frequencies over the focal sphere, and the ratio of *P*-to-*S* corner frequencies. Shear Mach waves lead to much higher corner frequency and scaled energy estimates locally, and as a result, up to a factor of 6–7 differences in corner frequencies can be seen over the focal sphere. The ratio of *S*-to-*P* radiated energy increases with the rupture speed in the subshear regime, whereas the ratio decreases with increasing rupture speed in the supershear regime.

From the source scenarios we have considered, we conclude that at least a factor of 2 difference in the spherical average of corner frequencies is expected in observational studies simply from variability in source geometry, rupture directivity, and rupture speeds, translating into a factor of 8 difference in estimated stress drops. Uncertainty in stress drop estimates due to unknown geometry and rupture speed also affects estimation of radiation efficiency. Our results further suggest that the large dependence of corner frequencies and scaled energy on takeoff angle relative to the source, which can be pronounced by rupture directivity, suggests that measurements from a small number of seismic stations are unlikely to produce unbiased estimates of spherically averaged corner frequency and energy. Furthermore, for asymmetrical ruptures, estimation of radiation efficiency may be less dependent on takeoff angle than either that of radiated energy or stress drop. However, accurate radiation efficiency estimates require independent constraints on the rupture speed and geometry.

Given the potential issues with stress drop and scaled energy estimates discussed in this work, one approach to better resolve earthquake source properties would be to observe the variations of corner frequencies or radiated energy over the focal sphere and relate them directly to theoretical models. For example, for a region with a dense seismic network, corner frequency variations over the focal sphere could be used to estimate how an earthquake source differs from a standard symmetrical circular model. Different patterns of corner frequencies or scaled energy over the focal sphere may provide additional insights into the complexities of earthquake source processes.

Appendix A: Stress Drop for an Elliptical Source

Stress drop for an elliptical source with the major and minor axes *a* and *b* can be derived from *Eshelby* [1957]. For a Poissonian solid (i.e., $\nu = 0.25$), *Madariaga* [1977] evaluated expressions for the stress drop in terms of the seismic moment (or average slip):

$$\Delta\sigma = \frac{M_0}{C_1 S b}, \tag{A1}$$

©2014. American Geophysical Union. All Rights Reserved.

where M_0 is the seismic moment, S is the source area, and the geometric parameter C_1. For slip along the major axis, C_1 is given by

$$C_1 = \frac{4}{3E(m) + \frac{1}{m^2}(E(m) - \frac{b^2}{a^2}K(m))}, \quad \text{(A2)}$$

where $m = (1 - b^2/a^2)^{1/2}$ and $K(m)$ and $E(m)$ are complete elliptical integrals of the first and second kinds, respectively [*Eshelby*, 1957; *Madariaga*, 1977]. We use equation (A1) to calculate stress drop for all the elliptical source scenarios.

Appendix B: Numerical Damping: Kelvin-Voight Viscosity

The Kelvin-Voight viscosity we use is artificial in the sense that it is part of the numerical procedure for solving the perfectly elastic problem and is not intended to represent physical damping. The purpose of the Kelvin-Voigt viscosity is to damp spurious oscillations generated by the fault slip at frequencies that are too high to be resolved by the mesh [e.g., *Day et al.*, 2005]. The viscosity η depends on the size of the elements on the fault and must be a small fraction of the critical time step in an elastic medium for the average linear size of the elements on the fault plane [e.g., *Ampuero*, 2002; *Kaneko et al.*, 2008]. Unless noted otherwise, we set $\eta = 0.1\Delta t$, where Δt is the time step used in a simulation. Values substantially larger than this value visibly degrade the sharpness with which shear stress is resolved at the rupture front.

Acknowledgments
We thank Rafael Benites for discussion on the analytical solution of stress drop for elliptical cracks. We also thank Anna Kaiser and Martin Vallee for helpful discussion. Comments by two anonymous reviewers helped us improve the manuscript. This work was supported by public research funding from the Government of New Zealand. We wish to acknowledge the contribution of NeSI high-performance computing facilities to the results of this research. New Zealand's national facilities are provided by the NZ eScience Infrastructure and funded jointly by NeSI's collaborator institutions and through the Ministry of Business, Innovation, and Employment Research Infrastructure program. Computer codes used in this work have been cited in the reference list and are available to anyone upon request.

References

Abercrombie, R. E. (1995), Earthquake source scaling relationships from −1 to 5 M_L using seismograms recorded at 2.5-km depth, *J. Geophys. Res.*, *100*(B12), 24,015–24,036, doi:10.1029/95JB02397.

Abercrombie, R. E., and J. R. Rice (2005), Can observations of earthquake scaling constrain slip weakening?, *Geophys. J. Int.*, *162*(2), 406–424, doi:10.1111/j.1365-246X.2005.02579.x.

Aki, K., and P. G. Richards (2002), *Quantitative Seismology*, University Science Books, Sausalito, Calif.

Allmann, B. B., and P. M. Shearer (2007), Spatial and temporal stress drop variations in small earthquakes near Parkfield, California, *J. Geophys. Res.*, *112*, B04305, doi:10.1029/2006JB004395.

Allmann, B. B., and P. M. Shearer (2009), Global variations of stress drop for moderate to large earthquakes, *J. Geophys. Res.*, *114*, B01310, doi:10.1029/2009JB005821.

Ampuero, J.-P. (2002), Etude physique et numérique de la nucléation des séismes, PhD thesis, Univ. Paris 7, Denis Diderot, Paris.

Andrews, D. J. (1976), Rupture velocity of plane strain shear cracks, *J. Geophys. Res.*, *81*, 5679–5687.

Andrews, D. J. (1985), Dynamic plane-strain shear rupture with a slip-weakening friction law calculated by a boundary integral method, *Bull. Seismol. Soc. Am.*, *75*, 1–21.

Andrews, D. J. (1986), Objective determination of source parameters and similarity of earthquakes of different size, in *Earthquake Source Mechanics, Geophys. Monogr. Ser.*, vol. 37, edited by S. Das, J. Boatwright, and C. H. Scholz, pp. 259–267, AGU, Washington, D. C.

Archuleta, R. J., E. Cranswick, C. Mueller, and P. Spudich (1982), Source parameters of the 1980 Mammoth Lakes, California, earthquake sequence, *J. Geophys. Res.*, *87*, 4595–4607, doi:10.1029/JB087iB06p04595.

Baltay, A., S. Ide, G. Prieto, and G. Beroza (2011), Variability in earthquake stress drop and apparent stress, *Geophys. Res. Lett.*, *38*, L06303, doi:10.1029/2011GL046698.

Bernard, P., and D. Baumont (2005), Shear Mach wave characterization for kinematic fault rupture models with constant supershear rupture velocity, *Geophys. J. Int.*, *162*, 431–447.

Boatwright, J. (1981), Quasi-dynamic models of simple earthquakes: Application to an aftershock of the 1975 Oroville, California, earthquake, *Bull. Seismol. Soc. Am.*, *71*(1), 69–94.

Brune, J. N. (1970), Tectonic stress and the spectra of seismic shear waves from earthquakes, *J. Geophys. Res.*, *75*, 4997–5009, doi:10.1029/JB075i026p04997.

Burridge, R. (1973), Admissible speeds for plane-strain shear cracks with friction but lacking cohesion, *Geophys. J. R. Astron. Soc.*, *35*, 439–455.

Burridge, R., and J. R. Willis (1969), The self-similar problem of the expanding elliptical crack in an anisotropic solid, *Proc. Cambridge Philos. Soc.*, *66*, 443–468.

Cotton, F., R. Archuleta, and M. Causse (2013), What is sigma of the stress drop?, *Seismol. Res. Lett.*, *84*(1), 42–48, doi:10.1785/0220120087.

Day, S. M., L. A. Dalguer, N. Lapusta, and Y. Liu (2005), Comparison of finite difference and boundary integral solutions to three-dimensional spontaneous rupture, *J. Geophys. Res.*, *110*, B12307, doi:10.1029/2005JB003813.

Dong, G., and A. S. Papageorgiou (2002a), Seismic radiation from a unidirectional asymmetrical circular crack model, Part I: Constant rupture velocity, *Bull. Seismol. Soc. Am.*, *92*, 945–961, doi:10.1785/0120000283.

Dong, G., and A. S. Papageorgiou (2002b), Seismic radiation from a unidirectional asymmetrical circular crack model, Part II: Variable Rupture Velocity, *Bull. Seismol. Soc. Am.*, *92*, 962–982, doi:10.1785/0120010209.

Dong, G., and A. S. Papageorgiou (2003), On a new class of kinematic models: Symmetrical and asymmetrical circular and elliptical cracks, *Phys. Earth Planet. Inter.*, *137*, 129–151.

Dunham, E. M., and H. S. Bhat (2008), Attenuation of radiated ground motion and stresses from three-dimensional supershear ruptures, *J. Geophys. Res.*, *113*, B08319, doi:10.1029/2007JB005182.

Eshelby, J. D. (1957), The determination of the elastic field of an ellipsoidal inclusion, and related problems, *Proc. R. Soc. London, Ser. A*, *241*(1226), 376–396.

Hanks, T. C., and W. Thatcher (1972), A graphical representation of seismic source parameters, *J. Geophys. Res.*, *77*(23), 4393–4405, doi:10.1029/JB077i023p04393.

©2014. American Geophysical Union. All Rights Reserved.

Harris, R. A., et al. (2009), The SCEC/USGS dynamic earthquake rupture code verification exercise, *Seismol. Res. Lett.*, *80*(1), 119–126, doi:10.1785/gssrl.80.1.119.
Harris, R. A., et al. (2011), Verifying a computational method for predicting extreme ground motion, *Seismol. Res. Lett.*, *82*(5), 638–644, doi:10.1785/gssrl.82.5.638.
Haskell, N. A. (1964), Total energy and energy spectral density of elastic wave radiation from propagating faults, *Bull. Seismol. Soc. Am.*, *54*(6A), 1811–1842.
Henry, C., and S. Das (2001), Aftershock zones of large shallow earthquakes: Fault dimensions, aftershock area expansion and scaling relations, *Geophys. J. Int.*, *147*, 272–293, doi:10.1046/j.1365-246X.2001.00522.x.
Ide, S., G. C. Beroza, S. G. Prejean, and W. L. Ellsworth (2003), Apparent break in earthquake scaling due to path and site effects on deep borehole recordings, *J. Geophys. Res.*, *108*, 2271, doi:10.1029/2001JB001617.
Imanishi, K., and W. L. Ellsworth (2006), Source scaling relationships of microearthquakes at Parkfield, CA, determined using the SAFOD pilot hole seismic array, in *Earthquakes: Radiated Energy and the Physics of Faulting*, edited by R. Abercrombie et al., pp. 81–90, AGU, Washington, D. C., doi:10.1029/170GM10.
Kanamori, H., and D. L. Anderson (1975), Theoretical basis of some empirical relations in seismology, *Bull. Seismol. Soc. Am.*, *65*, 1073–1095.
Kaneko, Y., and P. M. Shearer (2014), Seismic source spectra and estimated stress drop derived from cohesive-zone models of circular subshear rupture, *Geophys. J. Int.*, *197*, 1002–1015, doi:10.1093/gji/ggu030.
Kaneko, Y., N. Lapusta, and J.-P. Ampuero (2008), Spectral element modeling of spontaneous earthquake rupture on rate and state faults: Effect of velocity-strengthening friction at shallow depths, *J. Geophys. Res.*, *113*, B09317, doi:10.1029/2007JB005553.
Kaneko, Y., J.-P. Ampuero, and N. Lapusta (2011), Spectral-element simulations of long-term fault slip: Effect of low-rigidity layers on earthquake-cycle dynamics, *J. Geophys. Res.*, *116*, B10313, doi:10.1029/2011JB008395.
Komatitsch, D., and J.-P. Vilotte (1998), The spectral element method: An efficient tool to simulate the seismic response of 2D and 3D geological structures, *Bull. Seismol. Soc. Am.*, *88*, 368–392.
Kostrov, B. V. (1974), Seismic moment and energy of earthquakes and seismic flow of rock [Engl. Translation], *Izv., Acad. Sci., USSR, Phys. Solid Earth*, *1*, 23–40.
Ma, S., and R. J. Archuleta (2006), Radiated seismic energy based on dynamic rupture models of faulting, *J. Geophys. Res.*, *111*, B05315, doi:10.1029/2005JB004055.
Madariaga, R. (1976), Dynamics of an expanding circular fault, *Bull. Seismol. Soc. Am.*, *66*(3), 639–666.
Madariaga, R. (1977), Implications of stress-drop models of earthquakes for the inversion of stress drop from seismic observations, *Pure Appl. Geophys.*, *115*(1–2), 301–316.
Mayeda, K., and W. R. Walter (1996), Moment, energy, stress drop, and source spectra of western United States earthquakes from regional coda envelopes, *J. Geophys. Res.*, *101*, 11,195–11,208, doi:10.1029/96JB00112.
McGuire, J. J., L. Zhao, and T. H. Jordan (2002), Predominance of unilateral rupture for a global catalog of large earthquakes, *Bull. Seismol. Soc. Am.*, *92*(8), 3309–3317, doi:10.1785/0120010293.
Mello, M., H. S. Bhat, A. J. Rosakis, and H. Kanamori (2010), Identifying the unique ground motion signatures of supershear earthquakes: Theory and experiments, *Tectonophysics*, *493*, 297–326, doi:10.1016/j.tecto.2010.07.003.
Noda, H., N. Lapusta, and H. Kanamori (2013), Comparison of average stress drop measures for ruptures with heterogeneous stress change and implications for earthquake physics, *Geophys. J. Int.*, *193*, 1691–1712, doi:10.1093/gji/ggt074.
Oth, A., and A. E. Kaiser (2014), Stress release and source scaling of the 2010–2011 Canterbury, New Zealand, earthquake sequence from spectral inversion of ground motion data, *Pure Appl. Geophys.*, *171*, 2767–2782, doi:10.1007/s00024-013-0751-1.
Prejean, S. G., and W. L. Ellsworth (2002), Observations of earthquake source parameters at 2 km depth in the Long Valley Caldera, Eastern California, *Bull. Seismol. Soc. Am.*, *91*(2), 165–177, doi:10.1785/0120000079.
Prieto, G. A., P. M. Shearer, F. L. Vernon, and D. Kilb (2004), Earthquake source scaling and self-similarity estimation from stacking *P* and *S* spectra, *J. Geophys. Res.*, *109*, B08310, doi:10.1029/2004JB003084.
Sato, T., and T. Hirasawa (1973), Body wave spectra from propagating shear cracks, *J. Phys. Earth*, *21*, 415–431.
Shearer, P. M., G. A. Prieto, and E. Hauksson (2006), Comprehensive analysis of earthquake source spectra in Southern California, *J. Geophys. Res.*, *111*, B06303, doi:10.1029/2005JB003979.
Silver, P. (1983), Retrieval of source-extent parameters and the interpretation of corner frequency, *Bull. Seismol. Soc. Am.*, *73*(73), 1499–1511.
Snoke, J. A. (1987), Stable determination of (Brune) stress drops, *Bull. Seismol. Soc. Am.*, *77*(2), 530–538.
Stork, A. L., and H. Ito (2004), Source parameter scaling for small earthquakes observed at the Western Nagano 800-m-deep borehole, Central Japan, *Bull. Seismol. Soc. Am.*, *94*(5), 1781–1794, doi:10.1785/012002214.
Walter, W., K. Mayeda, R. Gok, and A. Hofstetter (2006), The scaling of seismic energy with moment: Simple models compared with observations, in *Earthquakes: Radiated Energy and the Physics of Faulting*, vol. 170, edited by R. E. Abercrombie et al., pp. 25–41, AGU, Washington, D. C.
Yamada, T., P. G. Okubo, and C. J. Wolfe (2010), Kiholo Bay, Hawai'i, earthquake sequence of 2006: Relationship of the main shock slip with locations and source parameters of aftershocks, *J. Geophys. Res.*, *115*, B08304, doi:10.1029/2009JB006657.
Yang, W., Z. Peng, and Y. Ben-Zion (2009), Variations of strain-drops of aftershocks of the 1999 Izmit and Duzce earthquakes around the Karadere-Duzce branch of the North Anatolian Fault, *Geophys. J. Int.*, *177*, 235–246, doi:10.1111/j.1365-246X.2009.04108.x.

©2014. American Geophysical Union. All Rights Reserved.